

# Case Studies of Developing East Pacific Easterly Waves

David J. Raymond and Carlos López-Carrillo  
Physics Department and Geophysical Research Center  
New Mexico Tech  
Socorro, NM 87801  
USA

Lucio López Cavazos  
Instituto Tecnológico y Estudios Superiores de Monterrey  
Campus Querétaro  
Querétaro, Qro.  
México

February 15, 2006

# Summary

This paper reports a study of developing east Pacific easterly waves observed during the summer of 1991 with aircraft in situ and radar data and geosynchronous infrared satellite imagery. The circulation and divergence profiles, surface momentum and entropy fluxes, as well as 700 mb and 975 mb saturated and actual equivalent potential temperatures were measured repeatedly for three disturbances which evolved into east Pacific hurricanes. As the disturbances develop, the level of maximum updraft mass flux decreases, which leads to increased convergence at low levels. This process appears to be coupled to an increase in the mid-level relative humidity, which in turn suppresses the development of convective downdrafts. Comparison of the respective tendencies of convergence and surface friction to spin up and spin down a developing disturbance suggest that friction is unimportant in the early stages of development. However, as the surface circulation develops, the two effects become comparable in magnitude if surface friction is deposited through a fairly deep layer of the troposphere. Our observations appear to rule out boundary layer Ekman balance in these developing systems, though more accurate observations of the eddy fluxes of absolute vorticity into such systems are needed to answer this question with certainty.

## 1 Introduction

Westward-moving tropical waves, commonly called easterly waves, are ubiquitous in the tropics. These waves have been most intensively studied over west Africa and the eastern tropical Atlantic (Carlson, 1969; Burpee, 1972, 1974, 1975; Reed, Norquist, and Recker, 1977; Norquist, Recker, and Reed, 1977), the Caribbean (Riehl, 1954; Shapiro, 1986; Shapiro, Stevens, and Ciesielski, 1988), and the western Pacific (Yanai, Nitta, Maruyama, and Hayashi, 1968; Wallace, 1971; Reed and Recker, 1971). However, the waves also exist in the eastern Pacific (Nitta and Takayabu, 1985; Tai and Ogura, 1987) and the Indian Ocean (Saha, Sanders, and Shukla, 1981).

Easterly waves typically have a cyclonic vortex at middle levels with a weak cold core below the vortex and a warm core above, as demanded by balanced dynamics. The vertical structure varies with the ambient shear (Holton, 1971). Waves over Africa, the Atlantic, and the Caribbean typically have the vorticity anomaly elongated into the form of a trough aligned in the northeast-southwest direction (Burpee, 1972, 1975; Shapiro, 1986).

East Pacific easterly waves can often be traced back to Africa (Rappaport and Mayfield, 1992). However, these waves apparently gain energy when they cross Central America and enter the eastern Pacific (Nitta and Takayabu, 1985). Why this happens is unknown.

More than 50 years ago it was discovered that some easterly waves amplify into tropical storms (Dunn, 1940). Indeed, the majority of east Pacific tropical storms appear to form this way (see, e. g., Rappaport and Mayfield, 1992). Once a disturbance becomes warm core at lower levels, the mechanism for further amplification by convective heating is clear (Emanuel, 1986). However, determining *which* waves will reach this stage is not an easy task. Zehr (1992) characterizes this as the *genesis problem*.

A wide variety of mechanisms for wave amplification and cyclogenesis have been suggested, but most boil down to some form of interaction of the wave with another atmospheric disturbance (see, e. g., Shapiro, 1977). Pfeffer (1956, 1958), Pfeffer and Challa (1981), and Challa and Pfeffer (1980, 1990) have emphasized the role of inward eddy transport of angular momentum at both lower and upper levels. Riehl (1948), Sadler (1976), Molinari and Vollaro (1989, 1990), Molinari, Skubis, and Vollaro (1995), and others have suggested that the interaction of an easterly wave with a nearby upper level trough could induce cyclogenesis, and Montgomery and Farrell (1993) have provided theoretical support for this hypothesis. McBride and Zehr (1981) showed that the primary differences between developing and nondeveloping systems in the Atlantic and the western Pacific were the existence of weak vertical shear and large cyclonic and anticyclonic relative vorticity at lower and upper levels respectively. Lee (1989a,b) found that disturbances intensified when a “wind surge” in the surrounding environment interacted with the disturbance. Zehr (1992) confirmed the earlier results of McBride and Zehr and Lee in an extensive study of west Pacific tropical cyclogenesis and further showed that spinup occurred impulsively in association with strong convective bursts. For the special case of east Pacific cyclones, Zehnder (1991) hypothesized that the mountains of Central America play a role in cyclogenesis by modifying waves impinging from the Caribbean in a manner favorable to development.

The TEXMEX (Tropical Experiment in México) project provided an opportunity to study the intensification of easterly waves and the associated tropical cyclogenesis in the eastern Pacific. This project employed two aircraft, one of the NOAA (National Oceanic and Atmospheric Administration) WP-3s and the NCAR (National Center for Atmospheric Research) Electra. These aircraft were deployed from Acapulco, México into developing east Pacific easterly waves during the summer of 1991. In situ data were obtained from both aircraft. Most importantly, the WP-3 carried an X-band Doppler radar. Geostationary satellite data were used operationally and employed subsequently to provide time continuity and background for the aircraft observations.

The purpose of this paper is to present case studies of developing easterly waves in the east Pacific. Three of these waves eventually developed into hurricanes. The first wave, which became hurricane Enrique, was in an early stage of development during the period in which we observed it. The second, which became hurricane Fefa, was observed after it had already become a weak tropical storm. The third wave evolved into hurricane Guillermo as we watched. These three waves taken together provide a broader picture of development than any of the cases taken separately. Two other disturbances were studied, a weak, non-developing wave, and the large but weak tropical storm Hilda.

IOP	Start (UTC)	End (UTC)	Flights	Comment
0	2020, 4 July	2333, 4 July	1 p3, 1 el	intercomparison
1	1818, 6 July	0030, 7 July	1 p3	nondeveloping MCC
2	2000, 12 July	2201, 14 July	2 p3, 2 el	hurricane Enrique
3	2004, 20 July	0528, 21 July	1 p3	nondeveloping vortex
4	2017, 28 July	0711, 30 July	2 p3, 1 el	hurricane Fefa
5	1002, 2 Aug	1605, 5 Aug	3 p3, 3 el	hurricane Guillermo
6	1801, 7 Aug	0400, 9 Aug	2 p3, 2 el	tropical storm Hilda

Table 1: Intensive observational periods (IOPs) for TEXMEX. The “Start” and “End” columns give the times respectively of the first takeoff and the last landing. Column 4 shows the number of WP-3 and Electra flights devoted to each IOP.

These disturbances weren’t well enough observed to contribute significantly to this work.

The order of presentation in this paper is as follows. Section 2 describes the TEXMEX project and the procedures for data analysis. Section 3 outlines how theoretical questions about tropical cyclogenesis can be addressed using our observations. An overview of east Pacific disturbances during the summer of 1991 is given in section 4. The case studies are presented in section 5. A synthesis of these observations is made in section 6, while the conclusions are summarized in section 7.

## 2 TEXMEX data analysis

The tropical eastern Pacific produces many tropical cyclones in a limited genesis region from  $95^\circ$  W to  $110^\circ$  W and  $10^\circ$  N to  $15^\circ$  N. This region is accessible to long range research aircraft from Acapulco, México (see Figure 1). Rappaport and Mayfield (1992) summarize the 1991 hurricane season in the eastern Pacific (the year in which TEXMEX took place), noting that 16 tropical cyclones developed, which is near the climatological average for this area. They also suggest that “. . . most, if not all, of the tropical cyclones formed from tropical waves first detected near the west coast of Africa.”

The TEXMEX project, which ran from the beginning of July through early August, 1991, was focused on the mechanism by which a cold core disturbance is converted into a warm core cyclone. Bister and Emanuel (1997) address this issue. However, sufficient observations were taken by the research aircraft to document the structure and short-term evolution of the predecessor cold core systems. We address these data in this paper.

### 2.1 In situ aircraft data

Table 1 shows the intensive observational periods (IOPs) for TEXMEX and the ultimate character of the target of the observations in each case. Note that 4 of the 7 IOPs

observed systems which ultimately developed into tropical storms. In IOPs 2, 4, and 5, aircraft were launched sequentially at 14 – 15 h intervals. In IOP 6 the WP-3 and the Electra were flown simultaneously at different altitudes. Extensive observations were taken at 700 mb in all but IOP 0. Observations were made at 200 – 300 m ASL in IOPs 2-6. In addition, observations were made at 850 mb and 490 mb in IOP 6. Ferry flights to and from the observational areas were usually flown near 500 mb, and sometimes provided useful data as well. For the purposes of this paper all aircraft data were smoothed with a low pass filter with a 10 s cutoff and then sampled at 10 s intervals.

The target area for each flight was decided upon by examining GOES-7 satellite loops for regions in which cloud motions indicated cyclonic rotation. It was found to be unprofitable to launch aircraft toward strong convective regions seen by satellite at pre-flight briefing time, as convection was often quite transient. However, rotation showed considerable continuity in time, and we were quite successful in launching aircraft into pre-cyclone circulations.

Equivalent potential temperatures are used frequently in this paper. All equivalent potential temperatures are computed according to the reversible formula (Emanuel, 1994), which reads about 8 degrees lower than the pseudoadiabatic formula at low levels in the moist tropics. Intercomparison flights at the beginning and end of the project show that the Electra and the WP-3 equivalent potential temperatures are within 1 K of each other from the surface to 550 mb. No attempt was made to further correct the data.

Winds are obtained via conventional techniques using airborne gust probe data combined with aircraft position and velocity measurements from the onboard inertial navigation system (INS). Unfortunately, the WP-3 lacked global positioning system (GPS) corrections to INS data, so computed aircraft winds are subject to the quasi-periodic Schuler oscillations of typical  $2 \text{ m s}^{-1}$  amplitude and 84 min period. The Electra was equipped with GPS and a composite aircraft velocity was computed by combining the low-pass-filtered part of the GPS velocity with the high-pass-filtered part of the INS velocity. This composite velocity is used to calculate the in situ winds.

## 2.2 Airborne radar data

Radar data from the NOAA WP-3 aircraft are synthesized using an extension of the method developed by Raymond and Lewis (1995) and by López (1995). The data are then objectively analyzed so as to fill in holes and smooth the results. Finally, a column divergence correction is done at each point for the purpose of computing vertical mass fluxes. Details of the analysis are given in the Appendix.

Figure 2 shows an example of the winds from the Doppler radar analysis before and after the objective analysis. This particular sample is nominally for winds at the surface. However, due to thresholding on gate elevation, only measurements between 0.5 km and 1 km are used. Without this thresholding, there are many grid points showing very weak winds, reflecting contamination by sea clutter. These points are mostly eliminated by

the thresholding. As is seen in figure 2, the objective analysis is effective in interpolating across holes in the radar data.

### 2.3 Satellite data

The GOES-7 geosynchronous satellite provided us with infrared and visible images during the TEXMEX project. Here we use only the infrared images. Hourly image data for the period of the TEXMEX project are interpolated to  $0.1^\circ \times 0.1^\circ$  area elements and converted to infrared brightness temperatures. These data are then used in a variety of ways. In one application we track each disturbance in the satellite imagery, following it with a  $5^\circ \times 5^\circ$  square window centered on the disturbance. The infrared brightness temperatures of the area elements in this window are histogrammed, resulting nominally in a vertical distribution of cloud top temperatures in the region of the disturbance. These histograms are averaged for 4 h periods and combined to form a history of the convection occurring in each disturbance.

## 3 Theoretical considerations

We now show how our data can be used to infer certain properties of the observed disturbances. First we develop the relationship between system circulation, divergence, and surface friction. Second, we show how sea-air fluxes can be estimated from radar data. Third, we briefly review the predictions of the boundary layer quasi-equilibrium theory of convective forcing over the tropical oceans.

### 3.1 Circulation and mass fluxes

The absolute circulation  $\Gamma_a$  around an observed system is computed from

$$\Gamma_a \equiv \Gamma + Af \equiv \oint_{\delta A} u_{tan} ds + Af = \int_A \left( \frac{\partial v}{\partial x} - \frac{\partial u}{\partial y} \right) dA + Af \quad (1)$$

where  $\Gamma$  is the relative circulation,  $A = A(z)$  is the radar-observed area of the system, which is a generally decreasing function of height,  $\delta A$  is the periphery of  $A$ ,  $ds$  is a line element on  $\delta A$ , and  $f$  is the Coriolis parameter. The relative circulation is obtained via Stokes' theorem by horizontally integrating the vertical component of relative vorticity. The objectively analyzed horizontal wind,  $\mathbf{u} = (u, v)$ , is used in this computation and  $u_{tan} = \mathbf{u} \cdot \mathbf{t}$  is the component of  $\mathbf{u}$  tangent to  $\delta A$  (see figure 3).

The detrained volume flux is

$$\Delta \equiv \oint_{\delta A} u_{out} ds = \int_A \left( \frac{\partial u}{\partial x} + \frac{\partial v}{\partial y} \right) dA \quad (2)$$

where  $u_{out} = \mathbf{u} \cdot \mathbf{n}$  and  $\mathbf{n}$  is a unit outward normal on  $\delta A$ . The divergence theorem is used to convert the line integral to a surface integral in the above equation.

The detrained mass flux is simply  $\Delta$  multiplied by the mass density  $\rho(z)$ . As noted in the Appendix, a column-by-column divergence correction is made such that

$$\int_0^{top} \rho \Delta dz = 0. \quad (3)$$

The net vertical mass flux is obtained by integrating the corrected  $\rho \Delta$ :

$$M(z) = - \int_0^z \rho \Delta dz'. \quad (4)$$

Clearly, these calculations miss contributions to the circulation and mass fluxes from motions outside the observable area of the system. However, the objective analysis largely fills in holes in the radar observations, especially below about 6 km, which is essential for relating the integrals of the divergence and vorticity to the detrained volume flux and the circulation.

The detrained volume flux and the time tendency of the absolute circulation can be related by the vorticity equation. Haynes and McIntyre (1987) write the equation for the vertical component of the absolute vorticity  $\zeta_a$  in pressure coordinates as follows:

$$\frac{\partial \zeta_a}{\partial t} + \frac{\partial Z_x}{\partial x} + \frac{\partial Z_y}{\partial y} = 0, \quad (5)$$

where  $Z_x$  and  $Z_y$  are the total isobaric fluxes of the vertical component of vorticity, and have the following form:

$$Z_x = u\zeta_a + \omega \frac{\partial v}{\partial p} - F_y \quad (6)$$

$$Z_y = v\zeta_a - \omega \frac{\partial u}{\partial p} + F_x, \quad (7)$$

where  $\omega$  is the pressure vertical velocity,  $p$  is the pressure, and  $F_x$  and  $F_y$  are the horizontal force components per unit mass due to eddy momentum fluxes.

The difference between pressure and geometric vertical coordinates is insignificant here, so we continue the development in geometric coordinates. Integrating (5) over some area  $A^*$  which is independent of height and time, but which is the minimal area that encompasses  $A(z)$  at all levels, we find after applying the divergence theorem that

$$\frac{d\Gamma_a^*}{dt} \equiv \frac{d}{dt} \int_{A^*} \zeta_a dA = - \oint_{\delta A^*} \mathbf{Z} \cdot \mathbf{n} ds \quad (8)$$

where  $\delta A^*$  is the periphery of  $A^*$  and  $\mathbf{Z} = (Z_x, Z_y)$  is the horizontal vorticity flux vector.

If the periphery of  $A^*$  is in clear air, then  $\omega$  is likely to be negligible there, and can be ignored. Thus,

$$\oint_{\delta A^*} \mathbf{Z} \cdot \mathbf{n} ds \approx \oint_{\delta A^*} (\zeta_a u_{out} - \mathbf{F} \cdot \mathbf{t}) ds \equiv \overline{\zeta_a} \Delta^* - \tau^*, \quad (9)$$

where  $\Delta^*$  is the volume flux detraining from area  $A^*$  and where

$$\bar{\zeta}_a \equiv \frac{1}{\Delta^*} \oint_{\delta A^*} \zeta_a u_{out} ds \quad (10)$$

is the weighted average of the absolute vorticity on the periphery of  $A^*$  with a weighting factor equal to the outflow component of the velocity  $u_{out}$ .

Combining this with (8) results in

$$\frac{d\Gamma_a^*}{dt} = -\bar{\zeta}_a \Delta^* + \tau^*, \quad (11)$$

which cleanly expresses the relationship between the rate of spinup of a system, the convergence of absolute vorticity into the system at each level, and the spindown tendency

$$\tau^* = \oint_{\delta A^*} \mathbf{F} \cdot \mathbf{t} ds \quad (12)$$

due to frictional forces.

To the extent that  $\Gamma_a \approx \Gamma_a^*$  and  $\Delta \approx \Delta^*$ , we have a tool for using observable quantities to explore the spinup of an easterly wave into a tropical storm. These assumptions are probably not too bad. The latter assumption is valid if the mean divergence in the clear region between  $\delta A$  and  $\delta A^*$  is small. This seems likely to be true on the average since this region by definition contains little or no precipitating convection. The validity of the former assumption is less obvious. However, at low levels the clear region is likely to be small in area, minimizing the error. At upper levels, the tendency of convective systems to detrain air of near-zero potential vorticity means that the difference between  $\Gamma_a$  and  $\Gamma_a^*$  should be small there as well.

### 3.2 Surface fluxes

Since we have approximate surface winds from the WP-3 radar observations, we can estimate the sea-air entropy fluxes in the observed disturbances. We define

$$F_e = C_d |\mathbf{u}| \delta \theta_e, \quad (13)$$

where  $\delta \theta_e \approx 20$  K is the saturated sea surface equivalent potential temperature minus the boundary layer equivalent potential temperature and  $C_d \approx 1.5 \times 10^{-3}$  is the bulk transfer coefficient. We further approximate the total heat flux as

$$F_h = (\rho_s C_p T / \theta_{eb}) F_e, \quad (14)$$

where  $\rho_s$  is the surface air density,  $C_p$  is the specific heat of air at constant pressure,  $T$  is the surface air temperature, and  $\theta_{eb}$  is the boundary layer equivalent potential temperature. The expression in parentheses is roughly  $1050 \text{ J m}^{-3} \text{ K}^{-1}$ .

Equation (11) needs an estimate of the drag force due to the eddy transfer of momentum to the surface. Since we don't know the vertical distribution of the action of

surface drag, we estimate the vertically averaged drag force per unit mass due to surface friction as

$$\mathbf{F} = -C_d|\mathbf{u}|\mathbf{u}/d, \quad (15)$$

where  $C_d \approx 1.5 \times 10^{-3}$  is assumed as before,  $d$  is the depth of the averaging region, and  $\mathbf{u}$  is the radar-derived low-level wind speed. Various hypotheses for the value of  $d$  may be made. We take  $d$  to be the depth of the inflow layer so that the surface stress is assumed to be distributed uniformly through this layer.

More accurate estimates of the surface exchange coefficients are available. However, the uncertainties in the other aspects of the calculation overwhelm the inaccuracies in our simple representation of these quantities.

### 3.3 Boundary layer quasi-equilibrium

In situ thermodynamic observations were made by both the Electra and WP-3 aircraft near 700 mb and 300 m ASL (nominally 975 mb). We concentrate on the observations of equivalent potential temperature and saturated equivalent potential temperature taken in the developing phases of Enrique, Guillermo, and Fefa. These are plotted as scatter plots versus the distance of the aircraft from the apparent center of the 700 mb vortex during each flight. Some data points are undoubtedly in error due to the wetting of the thermometer element during passage through cloud and rain. Wetting tends to reduce both the equivalent potential temperature and the saturated equivalent potential temperature. This needs to be kept in mind while interpreting the results. Examination of the relative humidity (not shown) suggests that not many of the data points were so contaminated.

Raymond (1995) and Emanuel (1995) proposed similar theories for the control of convection over tropical regions. The key element of the so-called *boundary layer quasi-equilibrium* theory is the idea that the governing factor is the budget of entropy in the atmospheric boundary layer. In a strongly convecting region this balance is primarily between the tendency of moist downdrafts to reduce the equivalent potential temperature of the boundary layer and the tendency of sea-air fluxes to increase it.

The downdraft entropy (or  $\theta_e$ ) flux is related to the updraft mass flux by cloud physical processes. Clouds with weak downdrafts, due perhaps to high relative humidity in the troposphere, should have a greater updraft mass flux for a given value of downdraft entropy flux.

An approximate formula for the cloud base updraft mass flux,  $M_u$ , appropriate to the convectively active region of an intensifying wave is

$$M_u = \frac{\rho_s \overline{F}_e}{\alpha \delta \theta_{em}}, \quad (16)$$

where  $\rho_s$  is the air density at the surface,  $\overline{F}_e$  is the average of  $F_e$  over the region of interest,  $\alpha \equiv M_d/M_u$  is the ratio of downdraft to updraft mass flux at cloud base, and

$\delta\theta_{em}$  is the equivalent potential temperature deficit of air imported into the boundary layer by convective downdrafts. This equation comes from the assumption that  $\rho_s \overline{F}_e$ , the mean surface flux of  $\theta_e$ , is balanced by  $M_d \delta\theta_{em} = \alpha M_u \delta\theta_{em}$ , the downdraft flux of  $\theta_e$  into the boundary layer. The justifications for this assumption in a convectively active region are presented in detail by Raymond (1995).

## 4 Overview

Figure 4 shows the infrared brightness temperature from GOES-7 averaged in latitude over the monsoon trough region. Diurnal fluctuations are averaged out. The four named tropical storms during the TEXMEX period plus one unnamed event are visible as colder than average regions. All are moving to the west with speeds of order  $6^\circ \text{ d}^{-1}$ .

Notice a rather peculiar behavior in figure 4: All disturbances with the possible exception of Fefa extrapolate backwards to strong convection in the  $80^\circ - 85^\circ \text{ W}$  longitude range, which corresponds to the Central American land mass. However, a gap in the deep convection always occurs in the  $85^\circ - 90^\circ \text{ W}$  longitude range. The correspondence with convection over Central America supports the idea that these disturbances come from the east and may well be associated with African easterly waves. However, the reason for the gap in deep convection just to the west of Central America is not known. Perhaps this simply reflects subsidence over the coastal region induced by solar heating of the nearby land.

Figures 5 - 8 show contour plots of the relative frequencies of brightness temperatures of  $0.1^\circ \times 0.1^\circ$  area elements in GOES-7 infrared satellite pictures in a  $5^\circ \times 5^\circ$  square following the precursors to the named disturbances shown in figure 4.

The most obvious feature of these plots is the existence of a strong diurnal cycle, with maximum numbers of cold area elements, and hence deep cloudiness, near 1200 h UTC, or about 0600 h local time (LT). This is consistent with previous observations of tropical oceanic rainfall (Gray and Jacobson, 1977) and cloud (Hendon and Woodberry, 1993). Curiously, the deepest cloud appears first, with a subsequent gradual warming of brightness temperatures. This probably reflects the rapid development of deep stratiform cloudiness from convection, which itself doesn't have a large infrared signature. The warming probably corresponds to the fallout and evaporation of the small ice crystals which make up the tops of the stratiform clouds. Similar behavior is seen by Chen, Houze, and Mapes (1996) in the equatorial western Pacific.

The diurnal cycle is undoubtedly related to the daily variation of insolation. Solar and infrared radiation have been shown to play a fairly strong role in tropical cyclone intensification (see, e. g., Craig, 1996), so the existence of such a cycle is not unexpected.

The other common feature is the development of a much higher fraction of cold cloud tops in these systems as they move to the west, with tops reaching above the 200 K level. This is correlated in each case except that of Hilda with the evolution into a tropical storm. The diurnal cycle also becomes suppressed, but doesn't disappear entirely, when the disturbances become hurricanes. Hilda, which was the only named system in this

sequence which didn't reach hurricane intensity, never produced cloud tops colder than 200 K, nor was the diurnal cycle suppressed.

By way of contrast, figure 9 shows the history of a non-developing, unnamed system studied during the one WP-3 flight of IOP-3. This system shows only minor and sporadic production of cold cloud tops, though hints of the diurnal cycle seen in the other systems still exist.

Measurements of sea surface temperature (SST) with the WP-3's downward pointing PRT-5 radiometer show that the ocean in the TEXMEX domain had nearly uniform temperatures of about 28° C, with somewhat higher temperatures occurring very near the Mexican coast. Thus, it seems unlikely that small scale spatial variations in SST were strong enough to exert significant differential effects between different developing systems during TEXMEX.

## 5 Case studies

We now present results on the vertical profiles of circulation, detrained volume flux, and vertical mass flux for three cases, Enrique (IOP-2), Guillermo (IOP-5) and Fefa (IOP-4). Each of these cases yields insight into different phases of the transformation of an easterly wave into a tropical cyclone. We also show the radial distributions of thermodynamic variables in these systems. The emphasis in all this work is on the bulk and radially symmetric aspects of these disturbances even though they were in general highly asymmetric.

### 5.1 Enrique

Enrique was observed at an early stage of its development. Figure 10 shows profiles of various radar-derived fields for the first WP-3 flight of IOP-2 (Enrique). Wind shear through the troposphere inside the system is of order 5 m s<sup>-1</sup>. Significant circulation is seen, with a maximum near 5 km elevation. However, the relative circulation near the surface is quite small at this stage. Little inflow appears to exist near the surface. The strongest net inflow is centered at 7 km elevation. Outflow is centered near 12 km. The vertical mass flux profile has a peak near 9 km elevation.

A little more than a day later the WP-3 made another flight through this wave, with the results shown in figure 11. At this point the circulation has increased by about 40%, still peaks near 4 – 5 km, and is much stronger near the surface. The mid-level inflow is centered near 6 km and the peak vertical mass flux is near 8 km. Surface inflow is non-existent in this case and significant detrainment near 2 km is evident. Shear of about 6 m s<sup>-1</sup> exists out of the north between 2 and 6 km at this stage.

In both of these cases the vertical mass flux profile is that which is expected in a stratiform rain region in which deep convection has ceased. Descent in the lower troposphere is topped by ascent in the upper troposphere (Houze, 1989).

Figures 12 and 13 show scatter plots of thermodynamic data as a function of radius for the 4 flights of IOP-2 at 700 mb and 975 mb. At 700 mb there is a tendency for the equivalent potential temperature to concentrate near 337 K, with a slight elevation near the vortex center in flight 4. However, near the surface there is a decreasing trend in equivalent potential temperature, from initial values near 350 K to typically 345 K or lower. Thus, the 975 mb – 700 mb difference decreases from about 13 K at the beginning to about 8 K at the end, primarily because of the decrease of surface values. This decrease is easily explained as a consequence of the downward transport of low equivalent potential temperature in downdrafts induced by the evaporation of precipitation.

The difference between the saturated and the actual equivalent potential temperature is a measure of relative humidity, and is thus presumably an indicator of the expected strength of downdrafts. Successive flights in IOP-2 generally show increasing convergence between equivalent potential temperature and saturated equivalent potential temperature values at 700 mb, indicating higher relative humidity, though flight 3 shows slightly less humidity than flight 2. This temporary decrease may be associated with the diurnal cycle.

## 5.2 Guillermo

Figure 14 shows the results of the second flight of IOP-5, which depicts the initial WP-3 penetration of the wave which became tropical storm Guillermo. (The first flight missed the wave trough completely.) The mid-level inflow is near 3-4 km elevation in this case and the surface inflow is slightly stronger than observed in Enrique. The updraft mass flux peaks at a rather low 6 km. The circulation is strongest near 4 km, but is still rather weak at the surface. Wind shear is quite weak through the troposphere.

The second WP-3 flight of IOP-5 is shown in figure 15. The circulation has increased by about 40% aloft, with a peak circulation near 4-5 km, as in the earlier flight. However, the surface circulation has increased even more. The detrained volume flux profile is similar to that in the earlier flight, though the peak in the vertical mass flux has risen to 7 km. The existence of some stratiform precipitation is indicated by the mid-level inflow. However, the vertical mass flux profile shows ascent at lower levels, which indicates that a significant convective component is active in the circulation (Houze, 1989).

Figure 16 shows the results from the third WP-3 flight into Guillermo. The structure of Guillermo changes dramatically between the second and third WP-3 flights into the system. The circulation is now nearly uniform from the surface to 14 km and inflow is maximal at the surface. The updraft mass flux peaks near 4 km elevation. The wind shear at the center of this system, which has now reached tropical storm stage, is minimal.

Figures 17 and 18 show the results of thermodynamic observations from flights 2-5 of IOP-5. In contrast with IOP-2, the equivalent potential temperature values at 700 mb and 975 mb are already 337 K and 345 K respectively at the start of observations, result-

ing in a consistent difference of about 8 K in equivalent potential temperature between the boundary layer and 700 mb. By the 5th flight the equivalent potential temperatures within 100 km of the center of the vortex are beginning to increase as Guillermo intensifies into a tropical storm.

The last panel of figures 21 and 22 show the 6th flight of IOP-5, when Guillermo is already a well developed tropical storm and is on the verge of becoming a hurricane. In this flight the difference between 975 mb and 700 mb equivalent potential temperatures has decreased even more, to about 6 K, and the system is strongly warm core in both temperature and equivalent potential temperature at both elevations. The relative humidity has increased to close to 100% and the size of the warm core has also increased.

### 5.3 Fefa

The first flight of IOP-4 caught Fefa at a stage of development superficially similar to that of Guillermo during WP-3 flight 4 into that system. However, unlike Guillermo, the surface circulation of Fefa is to the west of the 700 mb circulation by approximately 100 km. As the system develops, this westward displacement decreases.

As figure 19 shows, the low level inflow is significantly stronger in the Fefa case than it is in Guillermo at the comparison time. The vertical profile of vertical mass flux is stronger than Guillermo's and peaks at a lower level. The circulation profile is similar to Guillermo's at this stage. The wind shear is relatively weak.

Figure 20 shows the radar observations from the second WP-3 flight into Fefa. The convection is mainly on the east side of the system at this stage, which explains the strong shear seen in the mean radar winds. The maximum circulation is about the same as measured in the first WP-3 flight, though the circulation is slightly stronger at both lower and upper levels. The updraft mass flux is much weaker than in the first flight. However, it still shows a peak near 4 km. Fefa does not undergo much intensification between the first and second WP-3 flights, but tends to develop a circulation profile closer to that seen in the last Guillermo flight.

Figures 21 and 22 show thermodynamic measurements from the three flights of IOP-4. Fefa becomes significantly more of a warm core disturbance in this interval. However, the third flight shows that dry air has somehow penetrated to the core of Fefa, resulting in low equivalent potential temperatures there. It is noteworthy that the magnitude of the vertical mass flux has significantly decreased in this flight compared to that seen in the first flight. This may be a consequence of an increase in downdrafts associated with the drier air entering the core. During the third flight the circulation center at 700 mb is very near the western edge of the convection, resulting in less shielding of the core from environmental air. This may explain the ingestion of dry air by the core.

Comparison of Fefa's thermodynamic characteristics with the last IOP-5 flight in which Guillermo is a marginal hurricane is revealing. The Guillermo flight is seen in the lower right panel of figures 21 and 22. Notice that Guillermo is warm core in equivalent potential temperature at both 700 mb and 975 mb, and in temperature at 700 mb as

FLT	$d$	$\bar{\tau}$	$-f\bar{\Delta}$	$d\bar{\Gamma}_a/dt$
2-1	9 km	$-2 \text{ km}^2 \text{ ks}^{-2}$	$15 \text{ km}^2 \text{ ks}^{-2}$	$13 \text{ km}^2 \text{ ks}^{-2}$
2-3	8	-8	24	16
4-1	3	-38	69	31
4-3	3	-64	33	-31
5-2	6	-1	25	24
5-4	7	-14	16	2
5-6	4	-58	70	12

Table 2: Components  $\tau$  and  $-f\Delta$  of the circulation equation averaged over depth  $d$ , which is the depth of the inflow observed by radar in each WP-3 flight. The last column is the sum of the two previous columns.

well. Fefa only becomes warm core at 975 mb in flight 3. As discussed above, the warm core at 700 mb begins to develop in flight 2, only to collapse in flight 3 due to the probable intrusion of dry air, as discussed above.

## 6 Synthesis

We first attempt to understand how the circulation of these systems develops in the context of the vorticity equation, as described in the theory section. We then ask whether the theory of boundary layer quasi-equilibrium provides an explanation for the observed convection in these case studies. Finally we address the issue of the spinup of a tropical cyclone at upper levels.

### 6.1 Circulation tendency

Table 2 shows the friction and convergence terms on the right side of (11), averaged over the observed depth of the inflow in each case. An average over this depth is done because the vertical distribution of the action of surface drag is unknown. The final column is the sum of the previous two. Assuming that starred and unstarred quantities aren't too different, the last column gives an estimate of the rate of spinup or spindown of the system averaged over the depth of the inflow region. The divergence term assumes that air being ingested into the system has absolute vorticity equal to the Coriolis parameter  $f$ .

Though there are many uncertainties involved in the calculations of the results in table 2, they do lead to one conclusion. Early in the development of an easterly wave into a cyclone, surface friction has only a minor inhibiting effect on the spinup. This is because there is very little surface circulation at that time, and therefore little anticyclonic torque on the disturbance. Later in the development the convergence contribution increases,

but the frictional torque increases even more, to the point where the two effects are of the same order of magnitude.

An alternate way to increase the circulation is for the system to ingest air with a value of absolute vorticity greater than  $f$ . This is presumably related to the mechanism of spinup envisioned by Pfeffer (1956, 1958), Pfeffer and Challa (1981), and others, in which non-axisymmetric disturbances contrive to import angular momentum into a developing system. This sort of behavior may occur in at least one of the cases that we studied. Fefa appears to be interacting with a low level cyclonic shear line during flight 1 of IOP-4. This could have resulted in the ingestion of high vorticity air at low levels. Unfortunately, the point measurements of wind and vorticity needed to test this hypothesis are insufficiently accurate due to errors introduced by the Schuler oscillation of the inertial navigation system on the WP-3.

## 6.2 Ekman pumping

The assumption that the surface stress is uniformly distributed through the depth of the inflow layer is certainly the least justifiable ansatz in the entire analysis. An alternative hypothesis is that the effects of surface friction are confined to the atmospheric boundary layer (see the excellent paper by Ooyama, 1982). A near-balance is assumed to exist in this layer (taken to be 0.5-2 km thick) between the tendency of convergence to spin up the cyclone and the tendency of friction to spin it down. The boundary layer convergence is assumed to force deep convection. This is the Ekman pumping hypothesis.

The subsequent development of the cyclone is imagined to depend on the development of convergence in a *deep* tropospheric layer. This convergence is supposed to be the result of entrainment by the convection produced by Ekman pumping in the boundary layer. The convergence causes spinup in this layer, which lowers the surface pressure, thus increasing the tangential flow at the surface and strengthening the Ekman pumping.

The assumption of Ekman balance in the boundary layer is a hypothesis which is testable with our data. By assuming that all frictional stress is deposited in the boundary layer rather than in some deeper layer, we can calculate whether the approximate balance assumed between convergence and friction holds in the boundary layers of our systems.

Table 3 repeats the calculations of table 2 with the alternate assumption that all surface stress is deposited in the boundary layer, which is here assumed to be 1 km deep. Notice that the resulting spindown tendency from friction far exceeds the spinup tendency due to convergence in our sample. Therefore, the boundary layer Ekman pumping assumption is not even approximately valid in the storms we studied. In the strongest circulations the spindown tendency due to friction is about *four times* the spinup tendency due to convergence!

Our inability to determine whether air with absolute vorticity greater than  $f$  is systematically ingested into the disturbances causes some uncertainty in our conclusions. However, it seems unlikely that this effect could result in a four-fold increase in the spinup tendency.

FLT	$\bar{\tau}$	$-f\Delta$	$d\bar{\Gamma}_a/dt$
2-1	$-17 \text{ km}^2 \text{ ks}^{-2}$	$-3 \text{ km}^2 \text{ ks}^{-2}$	$-20 \text{ km}^2 \text{ ks}^{-2}$
2-3	-61	-4	-65
4-1	-114	80	-34
4-3	-193	46	-147
5-2	-8	10	2
5-4	-95	28	-67
5-6	-234	64	-170

Table 3: As in table 2 except that  $d = 1 \text{ km}$  assumed for all flights.

FLT	$A$	$\int_A F_e dA$	$\bar{F}_h$	$AM_{peak}/\rho_s$	$\alpha\delta\theta_{em}$	$\delta\theta_{e-700}$
2-1	151000	29000	202	895	32.4	7.2
2-3	173000	37000	225	759	48.7	5.5
4-1	136000	48000	371	7147	6.7	1.0
4-3	77000	45000	614	2525	17.8	2.4
5-2	145000	19000	138	2062	9.2	4.1
5-4	89000	24000	283	2388	10.1	4.6
5-6	111000	50000	473	5388	9.3	5.6

Table 4: Thermodynamic quantities computed for each WP-3 flight. See text for further explanation. The units of the various columns are as follows; Area  $A$ :  $\text{km}^2$ ;  $\int_A F_e dA$ :  $\text{km}^3 \text{ K ks}^{-1}$ ;  $\bar{F}_h$ :  $\text{W m}^{-2}$ ;  $AM_{peak}/\rho_s$ :  $\text{km}^3 \text{ ks}^{-1}$ ;  $\alpha\delta\theta_{em}$ :  $\text{K}$ ;  $\theta_{es} - \theta_e$ :  $\text{K}$ .

The assumption of confinement of friction to the sub-cloud layer seems naive based on what we know about convective momentum transfer — cumulus clouds can transfer momentum both up and down the gradient depending on their configuration (e. g., LeMone, 1983; LeMone, Barnes, and Zipser, 1984). We need to develop much better models of moist convective momentum transfer before we can understand its role in tropical cyclogenesis.

### 6.3 Convective forcing

A rigorous evaluation of the boundary layer quasi-equilibrium hypothesis requires separate estimates for the updraft and downdraft mass fluxes. This is not available from the current data set. It is therefore difficult to obtain a measurement of  $M_u$  at cloud base, since downdrafts are particularly strong at this level. However, the *peak* value of net mass flux may be a reasonable estimate of cloud base updraft flux if entrainment and detrainment in the updraft aren't too strong. Presumably at the level of maximum net vertical mass flux the downdraft mass flux is negligible. On this hypothesis we have inverted (16) for  $\alpha\delta\theta_{em}$  and computed it with the above assumption for  $M_u$ . The results

are shown in the 6th column of table 4.

If the updraft and downdraft mass flux balance each other at the surface, then  $\alpha = 1$ . Furthermore, in ordinary tropical conditions one might expect that  $\delta\theta_{em} \approx 10$  K, leading to an estimated value of  $\alpha\delta\theta_{em} \approx 10$  K. Inspection of table 4 shows that  $\alpha\delta\theta_{em}$  is typically not too far from this value. Larger values of  $\alpha\delta\theta_{em}$  are seen for the IOP-2 cases, but deep convection was apparently almost completely inactive when the WP-3 observed this system, which means that only upper tropospheric mesoscale motions were contributing to the updraft.

If a moist middle troposphere promotes fewer downdrafts, then there should be a positive correlation between the observed value of the difference between the saturated and actual equivalent potential temperature observed at 700 mb and the value of  $\alpha\delta\theta_{em}$  inferred from radar observations and the boundary layer quasi-equilibrium equation, (16). Figure 23 shows the averaged value  $\delta\theta_{e-700} \equiv \theta_{es} - \theta$  between 680 mb and 720 mb within 200 km of the disturbance center plotted versus  $\alpha\delta\theta_{em}$  for all WP-3 flights in IOPs 2, 4, and 5. Table 4 also shows these values. There is indeed a correlation between these two quantities, though significant scatter exists as well. The number of cases is not large, but these results suggest that moistening of the middle troposphere is important to the formation of large upward mass fluxes in developing tropical cyclones.

## 6.4 Spinup in the upper troposphere

The cyclonic circulation in Guillermo (as in most hurricanes) extends to high altitude where the flow is strongly divergent. How can this spinup be reconciled with the circulation tendency equation (11)? Since the boundary of the area  $A^*$  extends beyond region of active convection,  $\tau^*$  is likely to be zero there. Therefore, the only possible way in which spinup could occur within this area is if there is net inward transport of absolute vorticity at high levels. Satellite loops show that the flow at these levels is almost always uniformly outward once a system has begun to develop. In this case spinup at high levels can only happen if *air with negative absolute vorticity is being exported from the system*. Further work is needed to understand how this can happen, but it is likely to be associated with convective momentum transport in the core of the system, since this can generate the necessary separation of positive and negative potential vorticity (Raymond, 1992).

## 7 Conclusions

Observations taken during the TEXMEX project of developing easterly waves lead us to the following conclusions:

- The satellite infrared signatures of the observed east Pacific easterly waves extend eastward at least to Central America, though a gap exists in the far eastern Pacific adjacent to land.

- A strong diurnal cycle exists in the deep convection associated with these systems. The maximum in cold cloud occurs near local sunrise, as in other tropical oceanic regions. The diurnal cycle weakens and the coldest cloud tops develop when tropical cyclogenesis occurs.
- The Ekman pumping assumption of certain models, in which surface friction is confined to the boundary layer and nearly balances the tendency of convergence to spin up the system, appears to be inconsistent with our observations. Surface friction is calculated to be far too strong to be balanced by convergence if its effects are confined to, say, the lowest kilometer of the atmosphere.
- Early on, the circulation in these systems peaks near 5 km. The early stage of spinup of the observed systems is apparently only weakly affected by surface friction because the surface circulation at this point is weak. Later on surface friction becomes a significant drag on the system, even when the effects of friction are distributed through a deep tropospheric layer.
- Higher mid-tropospheric humidity appears to be correlated with a lower elevation of the maximum in vertical mass flux. There is also an indication of a correlation between higher relative humidity and the weakening of downdraft entropy fluxes, though much more evidence needs to be assembled on this point.

*Acknowledgments.* We thank Kerry Emanuel for inviting us to become involved in TEXMEX, and for the many stimulating discussions about tropical cyclogenesis. The aircraft research operations of both the National Center for Atmospheric Research and the National Oceanographic and Atmospheric Administration played an indispensable role in this project. We also thank the University Corporation for Atmospheric Research's Unidata project for their help in providing GOES satellite imagery to us. Bob Gall and the University of Arizona group provided an on-site McIDAS system that was crucial in defining aircraft missions. The National Hurricane Center and the staff of the Hurricane Research Division of NOAA provided excellent forecasts as well as guidance in flight planning. We particularly wish to thank Stan Rosenthal and Bob Burpee for their support of TEXMEX. Without the tremendous help of Odón Sánchez of ITESM-Querétaro, this project would not have been possible. Frank Marks and Dave Jorgensen were both very helpful with advice in the analysis of the WP-3 radar data. Melissa Griffin did an excellent job of analyzing the satellite data. Two anonymous reviewers made helpful suggestions. Finally, we thank Lalo McKissack of the Playa Hermosa hotel in Acapulco for his fine hospitality. This work was supported by NSF Grants ATM-8914116 and ATM-9311735 as well as NOAA Climate and Global Change Program Grant NA56GP0219.

## Appendix — Doppler radar analysis

In our method all of the radial velocity data from radar gates contributing to a Cartesian grid point are used in a least squares fit to produce the particle velocity vector

at that grid point. Data were interpolated to a Cartesian grid  $5 \text{ km} \times 5 \text{ km} \times 1 \text{ km}$  from the surface to 20 km.

The interpolation process worked as follows: Starting with raw radar data from the aircraft, reflectivities and velocities from each radar gate are assigned to each of the eight surrounding Cartesian grid points. At each grid point all assigned data are used to calculate the following sums:

$$A_{ij} = \sum_k W_k n_{ik} n_{jk} \quad i, j = x, y, z \quad (17)$$

$$B_i = \sum_k W_k n_{ik} V_{rk} \quad i = x, y \quad (18)$$

$$C_{ij} = \sum_k W_k^2 n_{ik} n_{jk} \quad i, j = x, y \quad (19)$$

where  $W_k$  is a weight inversely related to the distance of each radar gate point from the grid point to which it is assigned,  $n_{ik}$  is the direction cosine in the  $i$  direction of the ray associated with the  $k$ th gate point, and  $V_{rk}$  is the measured radial velocity at that point. Gate point positions are adjusted to a common time using an assumed constant translational velocity ( $U, V$ ) before these assignments are done. Values of  $U$  and  $V$  used for each case are shown in figures 10-19. Radial velocities also have the aircraft motion removed and are unfolded as described below. As a solution to the sea clutter problem, gates which have a nominal elevation above the sea surface of

$$z_m = z_{m0} + SR \quad (20)$$

or less are not used, where  $z_m = 0.5 \text{ km}$ ,  $R$  is the radar range in kilometers, and  $S = 2 \times 10^{-2}$ . This discards gates in which any part of the main beam, which has a spread of somewhat less than  $2^\circ$ , touches the sea surface. In addition, gates within 4 km of the aircraft are discarded due to contamination by strong specular side lobe reflections from the sea surface. First order corrections are made for the curvature of the Earth.

Unfolding is done before interpolation to a Cartesian grid by adding or subtracting twice the Nyquist velocity to the radial velocity at each gate until it most closely matches the radial velocity of the previous gate. The radial velocity at the first gate is unfolded by a similar process, but matching instead the in situ aircraft-determined wind. The in situ wind is first low pass filtered to remove small scale fluctuations which could upset this matching procedure. Little need was found to correct residual unfolding errors by hand.

As a result of the fitting procedure, the dual Doppler velocities are calculated as follows. First we define

$$u_{x0} = (B_x A_{yy} - B_y A_{xy})/D \quad u_{y0} = (B_y A_{xx} - B_x A_{xy})/D \quad (21)$$

and

$$g_x = (A_{xy} A_{yz} - A_{yy} A_{xz})/D \quad g_y = (A_{xy} A_{xz} - A_{xx} A_{yz})/D \quad (22)$$

where  $D = A_{xx}A_{yy} - A_{xy}^2$ . The variables  $u_{x0}$  and  $u_{y0}$  are the horizontal winds assuming that the vertical particle velocity is zero, whereas  $g_x$  and  $g_y$  are quantities used to later correct for non-zero vertical particle velocity.

Four error measures are also computed:

$$E_{rx} = (A_{yy}^2 C_{xx} - 2A_{yy}A_{xy}C_{xy} + A_{xy}^2 C_{yy})/D^2 \quad (23)$$

$$E_{ry} = (A_{xy}^2 C_{xx} - 2A_{xx}A_{xy}C_{xy} + A_{xx}^2 C_{yy})/D^2 \quad (24)$$

$$E_{px} = [(A_{xz}A_{yy} - A_{yz}A_{xy})/D]^2 \quad (25)$$

$$E_{py} = [(A_{yz}A_{xx} - A_{xz}A_{xy})/D]^2 \quad (26)$$

The first two of these are measures of the quality of the dual Doppler geometry, while the second two show the sensitivity of the calculated horizontal velocities to errors in the determination of the vertical particle velocity. We generally found it sufficient to impose the conditions  $E_{rx}, E_{ry} < 0.3$  and  $E_{px}, E_{py} < 1$  after interpolation to the Cartesian grid.

Occasional large spurious velocities slip through the analysis. These are generally the result of isolated unfolding problems. In order to minimize their impact on the subsequent analysis, we remove velocities with absolute component values in excess of  $25 \text{ m s}^{-1}$ . This threshold does not affect valid observations since the winds in the observed systems are almost always less than  $25 \text{ m s}^{-1}$ . The results we obtain are not sensitive to this thresholding value.

The true horizontal wind,  $(u, v)$ , is calculated for non-zero vertical particle velocity  $w_p$  using the following equations:

$$u = u_{x0} + g_x w_p \quad v = u_{y0} + g_y w_p. \quad (27)$$

The difficulty is then to obtain an estimate of  $w_p$ . This involves two steps, estimating the particle terminal velocity,  $w_t$ , and computing the vertical wind,  $w$ . From these two variables we get the vertical particle velocity using  $w_p = w - w_t$ . The terminal velocity is estimated from the radar reflectivity and the elevation using the algorithm of Jorgensen, LeMone, and Jou (1991). The vertical wind is obtained by integrating the continuity equation

$$\frac{1}{\rho} \frac{\partial \rho w}{\partial z} = -\frac{\partial}{\partial x}(u_{x0} + g_x w_p) - \frac{\partial}{\partial y}(u_{y0} + g_y w_p) \quad (28)$$

downward from cloud top where we assume  $w = 0$ . Since  $w$  is implicitly present on the right side of this equation via the term  $w_p$ , this is technically not a simple problem of integration, but involves the solution of a hyperbolic partial differential equation. This is done rather crudely using forward differencing in  $z$  so that  $w$  at a certain level is assumed to depend on  $w_p$  and hence  $w$  only at the next level up. The errors are small as long as the majority of the radar rays entering the calculation possess low elevation angles.

After the calculation of the Cartesian wind components, we then perform a simple objective analysis of the wind data in order to develop smoothed mesoscale wind

fields without holes due to missing data. At each elevation, each grid point is taken as the weighted average of raw data values within a specified radius of influence at that elevation. The weighting factor is taken to be

$$F = \frac{r - r_0}{r + r_0} \quad r \leq r_0, \quad (29)$$

where  $r$  is the distance between the grid point and the raw data value and  $r_0$  is the radius of influence. We take  $r_0 = 75$  km and also specify that a minimum of 30 good data points be within this radius for the result at a grid point to be considered valid. From these smoothed fields we calculate horizontal divergence and vorticity. Horizontally integrating these variables results in the detrained volume flux,  $\Delta$ , and the circulation,  $\Gamma$ , of the observed system as a function of height,  $z$ . A column divergence correction is done individually on each column after the smoothing but before the integration to correct divergence errors introduced by the objective analysis.

Since GPS correction of the INS aircraft velocity was not available on the NOAA WP-3 at the time of TEXMEX, we were concerned about the errors introduced into the detrained volume flux and the circulation by the Schuler oscillation of the INS-derived aircraft velocity. We tested the sensitivity of these calculations to the introduction of an added artificial oscillation of amplitude  $2 \text{ m s}^{-1}$  and period 84 min. Typical errors in  $\Gamma$  are found to be of order  $10^3 \text{ km}^2 \text{ ks}^{-1}$  for the cases observed here. This is normally only 10-20% of the observed circulation values. Since the Schuler oscillation affects the divergence at all levels in a column in the same way, the column divergence correction eliminates this error.

## References

- Bister, M., and K. A. Emanuel, 1997: The genesis of hurricane Guillermo: TEXMEX analyses and a modeling study. *Mon. Wea. Rev.*, **125**, 2662-2682.
- Burpee, R. W., 1972: The origin and structure of easterly waves in the lower troposphere of North Africa. *J. Atmos. Sci.*, **29**, 77-90.
- Burpee, R. W., 1974: Characteristics of the North African easterly waves during the summers of 1968 and 1969. *J. Atmos. Sci.*, **31**, 1556-1570.
- Burpee, R. W., 1975: Some features of synoptic-scale waves based on compositing analysis of GATE data. *Mon. Wea. Rev.*, **103**, 921-925.
- Carlson, T. N., 1969: Some remarks on African disturbances and their progress over the tropical Atlantic. *Mon. Wea. Rev.*, **97**, 716-726.
- Challa, M., and R. L. Pfeffer, 1980: Effects of eddy fluxes of angular momentum on model hurricane development. *J. Atmos. Sci.*, **37**, 1603-1618.

- Challa, M., and R. L. Pfeffer, 1990: Formation of Atlantic hurricanes from cloud clusters and depressions. *J. Atmos. Sci.*, **47**, 909-927.
- Chen, S. S., R. A. Houze Jr., and B. E. Mapes, 1996: Multiscale variability of deep convection in relation to large-scale circulation in TOGA COARE. *J. Atmos. Sci.*, **53**, 1380-1409.
- Craig, G. C., 1996: Numerical experiments on radiation and tropical cyclones. *Quart. J. Roy. Meteor. Soc.*, **122**, 415-422.
- Craig, G. C., and S. L. Gray, 1996: CISK or WISHE as the mechanism for tropical cyclone intensification. *J. Atmos. Sci.*, **53**, 3528-3540.
- Dunn, G. E., 1940: Cyclogenesis in the tropical Atlantic. *Bull. Am. Meteor. Soc.*, **21**, 215-229.
- Emanuel, K. A., 1986: An air-sea interaction theory for tropical cyclones. Part I: Steady state maintenance. *J. Atmos. Sci.*, **43**, 585-604.
- Emanuel, K. A., 1994: *Atmospheric convection*. Oxford, 580 pp.
- Emanuel, K. A., 1995: The behavior of a simple hurricane model using a convective scheme based on subcloud-layer entropy equilibrium. *J. Atmos. Sci.*, **52**, 3960-3968.
- Gray, W. M., and R. W. Jacobson, Jr., 1977: Diurnal variation of deep convection. *Mon. Wea. Rev.*, **105**, 1171-1188.
- Haynes, P. H., and M. E. McIntyre, 1987: On the evolution of vorticity and potential vorticity in the presence of diabatic heating and frictional or other forces. *J. Atmos. Sci.*, **44**, 828-841.
- Hendon, H. H., and K. Woodberry, 1993: The diurnal cycle of tropical convection. *J. Geophys. Res.*, **98**, 16623-16637.
- Holton, J., 1971: A diagnostic model for equatorial wave disturbances: The role of vertical shear of the mean zonal wind. *J. Atmos. Sci.*, **28**, 55-64.
- Houze, R. A., Jr., 1989: Observed structure of mesoscale convective systems and implications for large-scale heating. *Quart. J. Roy. Meteor. Soc.*, **115**, 425-461.
- Jorgensen, D. P., M. A. LeMone, and B. J.-D. Jou, 1991: Precipitation and kinematic structure of an oceanic mesoscale convective system. Part I: convective line structure. *Mon. Wea. Rev.*, **119**, 2608-2637.
- Lee, C. S., 1989a: Observational analysis of tropical cyclogenesis in the western north Pacific. Part I: structural evolution of cloud clusters. *J. Atmos. Sci.*, **46**, 2580-2598.

- Lee, C. S., 1989b: Observational analysis of tropical cyclogenesis in the western north Pacific. Part II: budget analysis. *J. Atmos. Sci.*, **46**, 2599-2616.
- LeMone, M. A., 1983: Momentum transport by a line of cumulonimbus. *J. Atmos. Sci.*, **40**, 1815-1834.
- LeMone, M. A., G. M. Barnes, and E. J. Zipser, 1984: Momentum flux by lines of cumulonimbus over the tropical oceans. *J. Atmos. Sci.*, **41**, 1914-1932.
- López, L., 1995: *Precipitation development in convective systems over the west Pacific warm pool*. PhD dissertation, New Mexico Institute of Mining and Technology, Socorro, NM, 144 pp.
- McBride, J. L., and R. Zehr, 1981: Observational analysis of tropical cyclone formation. Part II: comparison of nondeveloping versus developing systems. *J. Atmos. Sci.*, **38**, 1132-1151.
- Molinari, J., S. Skubis, and D. Vollaro, 1995: External influences on hurricane intensity: Part III. Potential vorticity structure. *J. Atmos. Sci.*, **52**, 3593-3606.
- Molinari, J., and D. Vollaro, 1989: External influences on hurricane intensity: Part I. Outflow layer eddy angular momentum fluxes. *J. Atmos. Sci.*, **46**, 1093-1105.
- Molinari, J., and D. Vollaro, 1990: External influences on hurricane intensity: Part II. Vertical structure and response of the hurricane vortex. *J. Atmos. Sci.*, **47**, 1902-1918.
- Montgomery, M. T., and B. F. Farrell, 1993: Tropical cyclone formation. *J. Atmos. Sci.*, **50**, 285-310.
- Nitta, T., and Y. Takayabu, 1985: Global analysis of the lower tropospheric disturbances in the tropics during the northern summer of the FGGE year. Part II: Regional characteristics of the disturbances. *Pure Appl. Geophys.*, **123**, 272-292.
- Norquist, D. C., E. E. Recker, and R. J. Reed, 1977: The energetics of African wave disturbances as observed during Phase III of GATE. *Mon. Wea. Rev.*, **105**, 334-342.
- Ooyama, K., 1982: Conceptual evolution of the theory and modeling of the tropical cyclone. *J. Meteor. Soc. Japan*, **60**, 369-379.
- Pfeffer, R. L., 1956: A discussion of the balance of angular momentum in hurricanes. *Bull. Am. Meteor. Soc.*, **37**, 234.
- Pfeffer, R. L., 1958: Concerning the mechanics of hurricanes. *J. Meteor.*, **15**, 113-120.

- Pfeffer, R. L., and M. Challa, 1981: A numerical study of the role of eddy fluxes of momentum in the development of Atlantic hurricanes. *J. Atmos. Sci.*, **38**, 2393-2398.
- Rappaport, E. N., and M. Mayfield, 1992: Eastern north Pacific hurricane season of 1991. *Mon. Wea. Rev.*, **120**, 2697-2708.
- Raymond, D. J., 1992: Nonlinear balance and potential-vorticity thinking at large Rossby number. *Quart. J. Roy. Meteor. Soc.*, **118**, 987-1015.
- Raymond, D. J., 1995: Regulation of moist convection over the west Pacific warm pool. *J. Atmos. Sci.*, **52**, 3945-3959.
- Raymond, D. J., and S. A. Lewis, 1995: Rotating convective disturbances in the trades. *Quart. J. Roy. Meteor. Soc.*, **121**, 271-299.
- Reed, R. J., D. C. Norquist, and E. E. Recker, 1977: The structure and properties of African wave disturbances as observed during Phase III of GATE. *Mon. Wea. Rev.*, **105**, 317-333.
- Reed, R. J. and E. E. Recker, 1971: Structure and properties of synoptic-scale wave disturbances in the equatorial western Pacific. *J. Atmos. Sci.*, **28**, 1117-1133.
- Riehl, H., 1948: On the formation of typhoons. *J. Meteor.*, **5**, 247-264.
- Riehl, H., 1954: *Tropical meteorology*. McGraw-Hill, 392 pp.
- Sadler, J. C., 1976: A role of the tropical upper tropospheric trough in early season typhoon development. *Mon. Wea. Rev.*, **104**, 1266-1278.
- Saha, K., F. Sanders, and J. Shukla, 1981: Westward propagating predecessors of monsoon depressions. *Mon. Wea. Rev.*, **109**, 330-343.
- Shapiro, L. J., 1977: Tropical storm formation from easterly waves: A criterion for development. *J. Atmos. Sci.*, **34**, 1007-1021.
- Shapiro, L. J., 1986: The three-dimensional structure of synoptic-scale disturbances over the tropical Atlantic. *Mon. Wea. Rev.*, **114**, 1876-1891.
- Shapiro, L. J., D. E. Stevens, and P. Ciesielski, 1988: A comparison of observed and model-derived structures of Caribbean easterly waves. *Mon. Wea. Rev.*, **116**, 921-938.
- Tai, K.-S., and Y. Ogura, 1987: An observational study of easterly waves over the eastern Pacific in the northern summer using FGGE data. *J. Atmos. Sci.*, **44**, 339-361.

- Wallace, J. M., 1971: Spectral studies of tropospheric wave disturbances in the tropical western Pacific. *Rev. Geophys. Space Phys.*, **9**, 557-612.
- Yanai, M., T. Nitta, T. Maruyama, Y. Hayashi, 1968: Power spectra of large-scale disturbances over the tropical Pacific. *J. Meteor. Soc. Japan*, **46**, 308-323.
- Zehnder, J. A., 1991: The interaction of planetary-scale tropical easterly waves with topography: A mechanism for the initiation of tropical cyclones. *J. Atmos. Sci.*, **48**, 1217-1230.
- Zehr, R. M., 1992: Tropical cyclogenesis in the western north Pacific. NOAA technical report NESDIS 61, 181 pp (Available from Dept. of Atmospheric Sciences, Colorado State University, Fort Collins, CO.).

## Figures

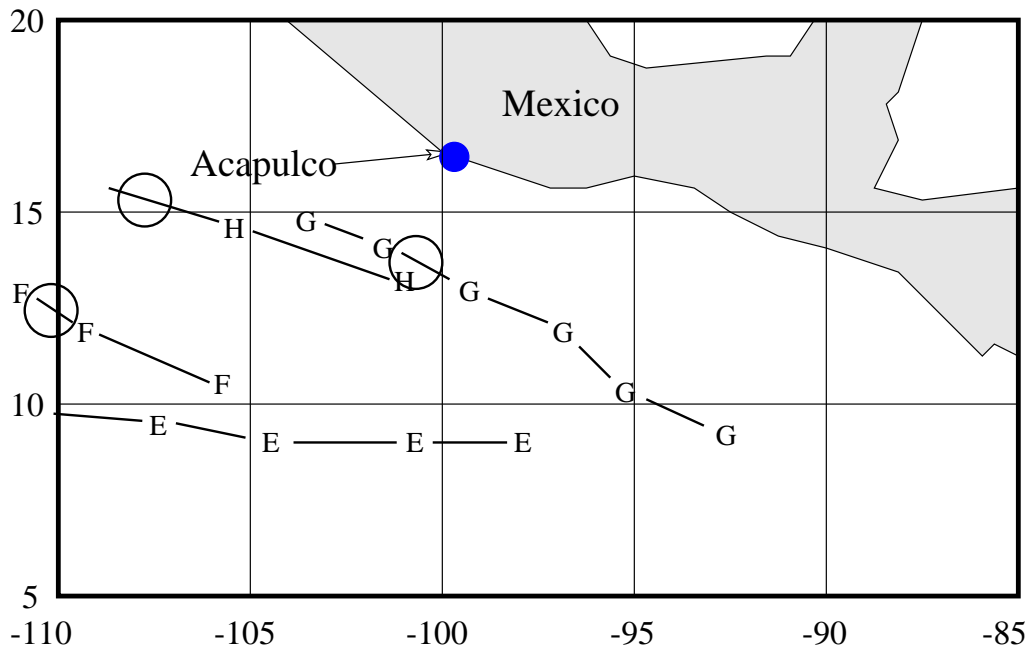


Figure 1: Map of the region of intensive cyclogenesis in the eastern Pacific. The letters connected by heavy lines show the aircraft-estimated vortex centers at roughly 14 h intervals of the disturbances that became tropical storms. Each letter is the first letter of the name of the corresponding storm. The circles show where each disturbance was declared a tropical storm by the National Hurricane Center. (Enrique was declared a tropical storm near 115° W.)

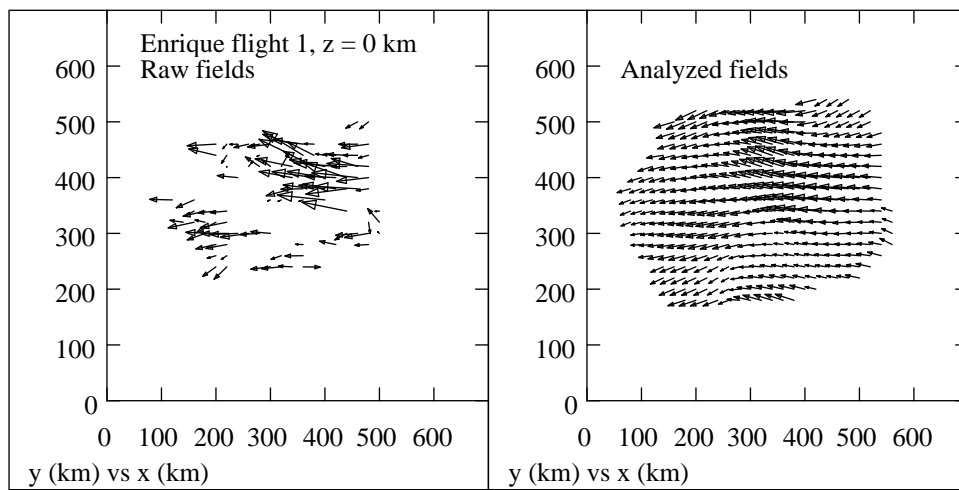


Figure 2: Nominal surface winds in Enrique for the first flight of IOP-2. The left panel shows the winds after interpolation to a grid but before the objective analysis. The right panel shows the winds after the objective analysis. For clarity the vectors have been thinned to one every 20 km in the  $x$  and  $y$  directions. The velocity scale is  $20 \text{ m s}^{-1}$  per 100 km.

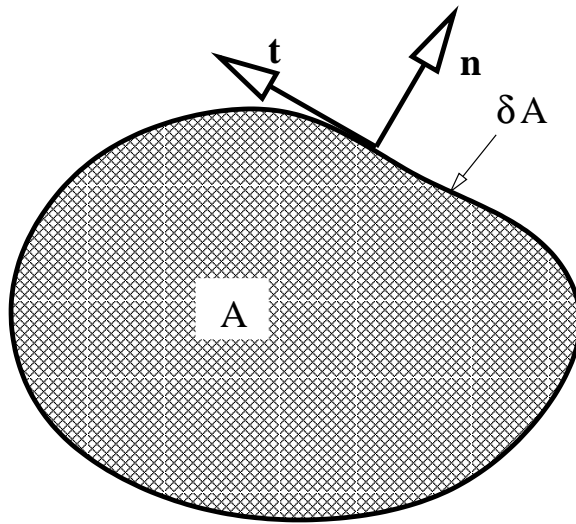


Figure 3: Definition sketch for circulation and detrained volume flux integrals.

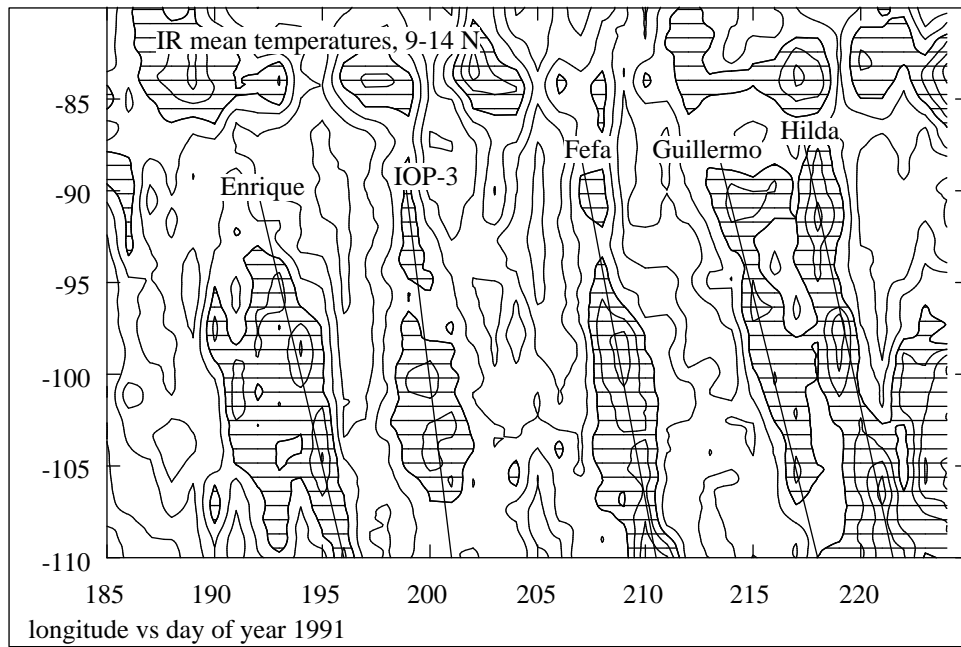


Figure 4: Infrared brightness temperature from GOES-7 averaged over the latitude range  $9^{\circ} - 14^{\circ}$ . The contour interval is 10 K and horizontal hatching indicates temperatures less than 260 K. The four named storms and the unnamed event of IOP-3 are visible in this presentation.

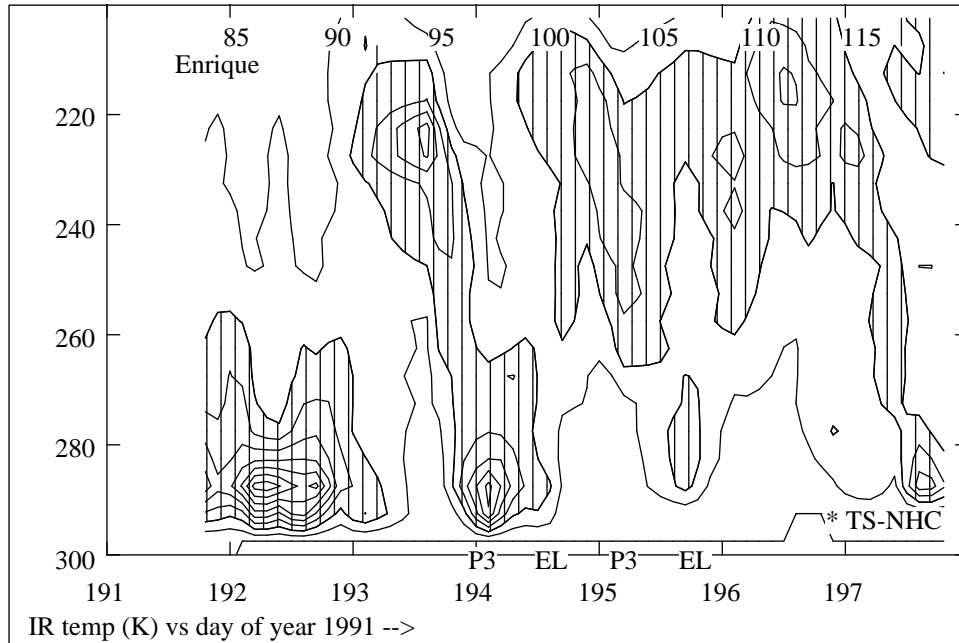


Figure 5: Contour plot of the relative frequency of GOES satellite pixels as a function of brightness temperature and time within a  $5^\circ \times 5^\circ$  square following the disturbance which became tropical storm Enrique (IOP-2). The contour interval is 0.125 with hatching where the relative frequency exceeds 0.25. The scaling of relative frequency is arbitrary. The numbers across the top indicate when the disturbance crossed the indicated longitude. The symbols EL and P3 along the bottom show the approximate times of Electra and WP-3 missions. The asterisk preceding “TS-NHC” indicates the approximate time at which the National Hurricane Center declared the system a tropical storm.

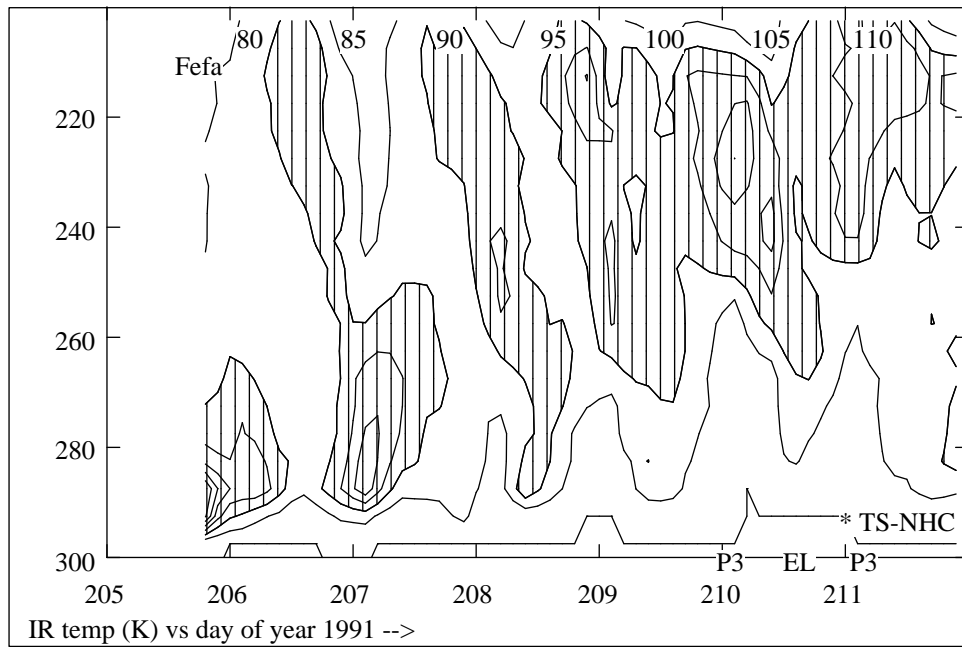


Figure 6: As in figure 5 except for the disturbance which became tropical storm Fefa (IOP-4).

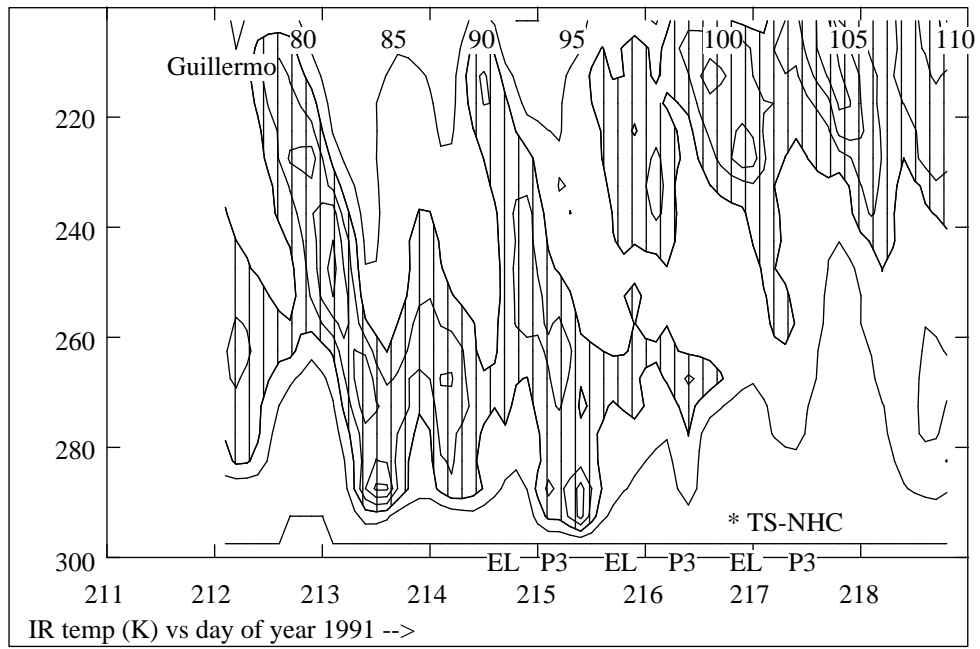


Figure 7: As in figure 5 except for the disturbance which became tropical storm Guillermo (IOP-5).

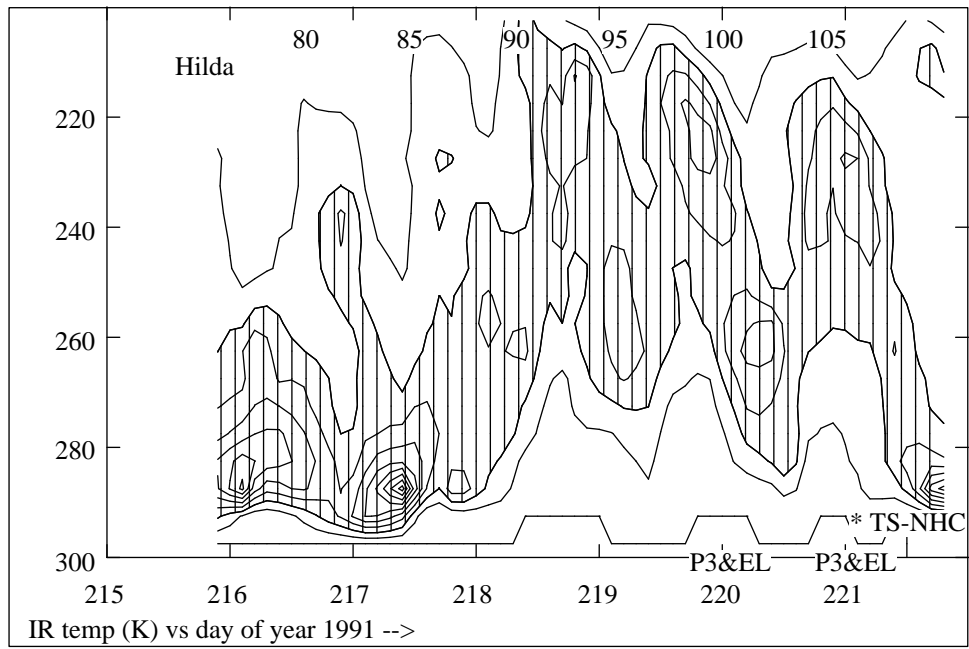


Figure 8: As in figure 5 except for the disturbance which became tropical storm Hilda (IOP-6).

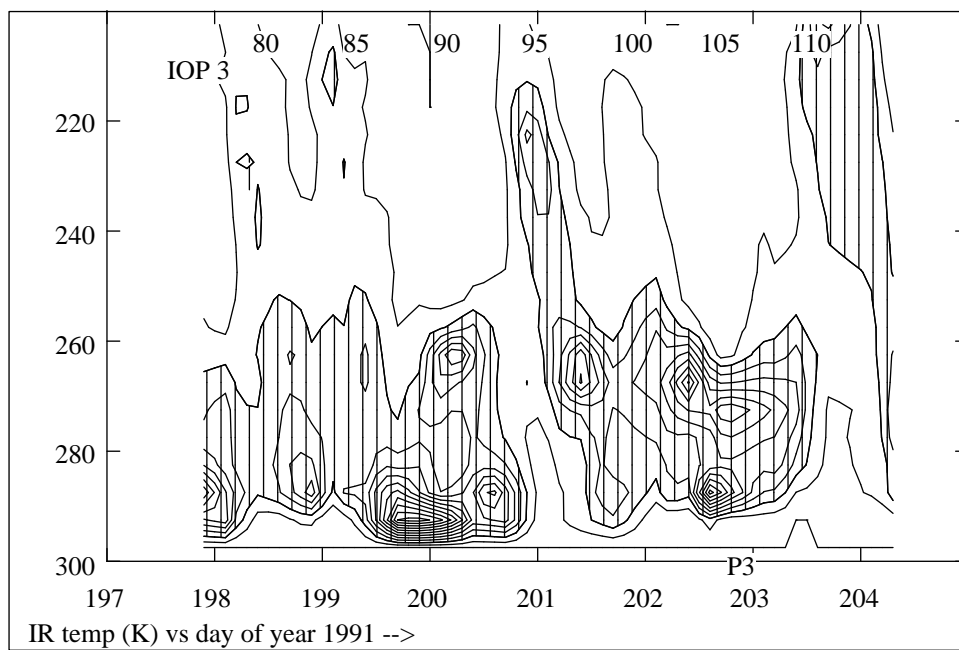


Figure 9: As in figure 5 except for the non-developing disturbance of IOP-3.

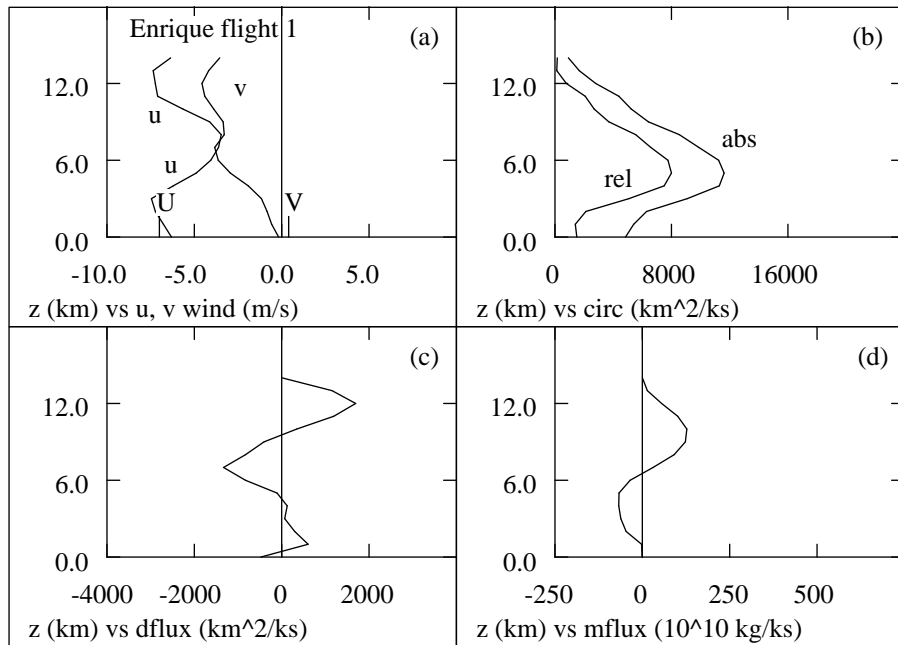


Figure 10: Vertical profiles of various radar-observed quantities for the first flight of IOP-2, near day 194.0. (a) Mean radar wind profiles. The assumed translational velocity is indicated by  $U$  and  $V$ . (b) Observed relative ( $\Gamma$ ) and absolute ( $\Gamma_a$ ) circulations. (c) Detrained volume flux ( $\Delta$ ). (d) Vertical mass flux ( $M$ ).

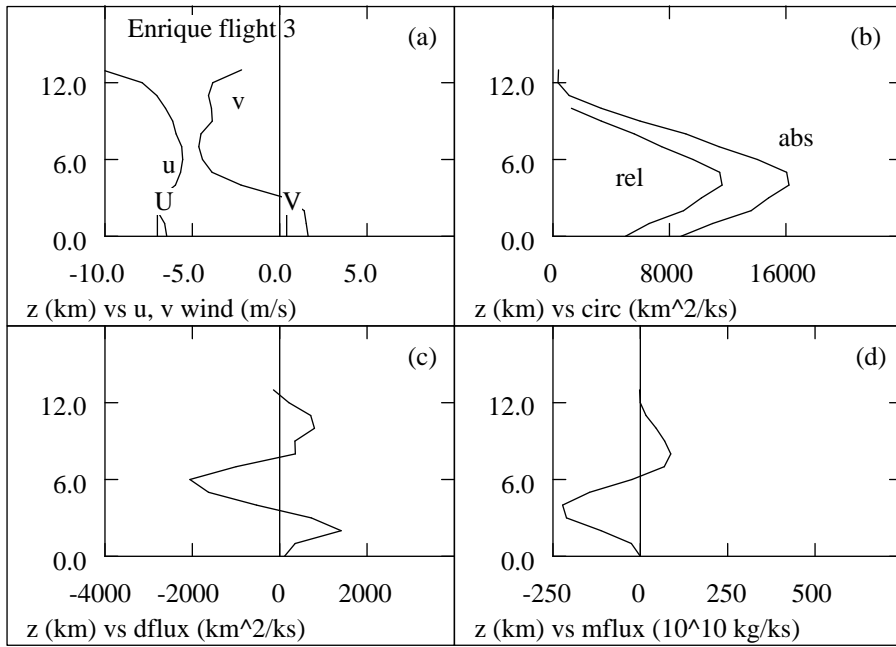


Figure 11: As in figure 10, except flight 3 of IOP-2, near day 195.2.

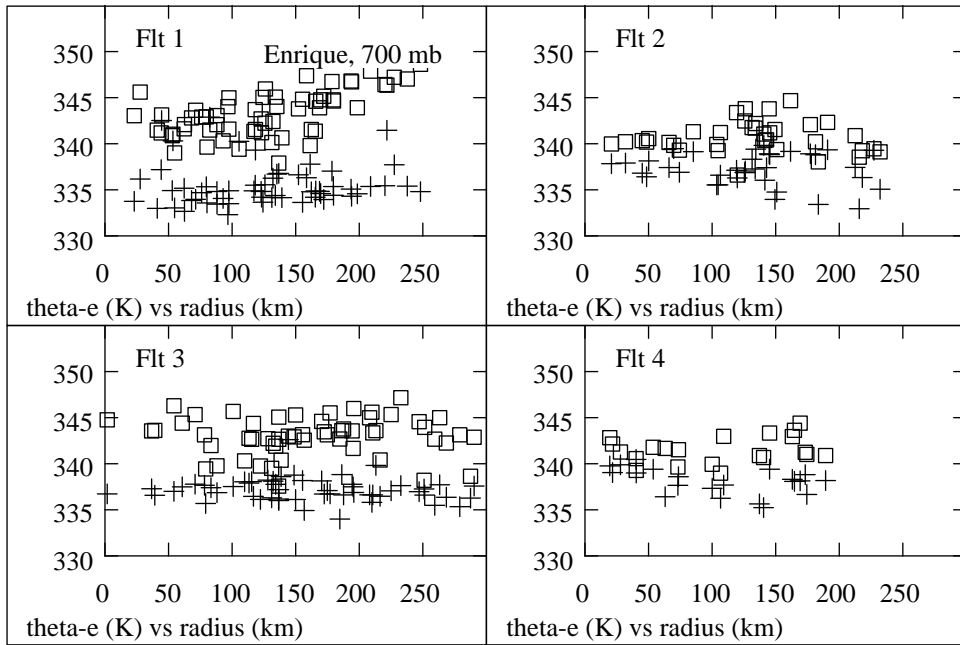


Figure 12: Scatter plot of equivalent potential temperature (crosses) and saturated equivalent potential temperature (squares) at 700 mb as a function of distance from the vortex center for flights 1-4 of IOP-2.

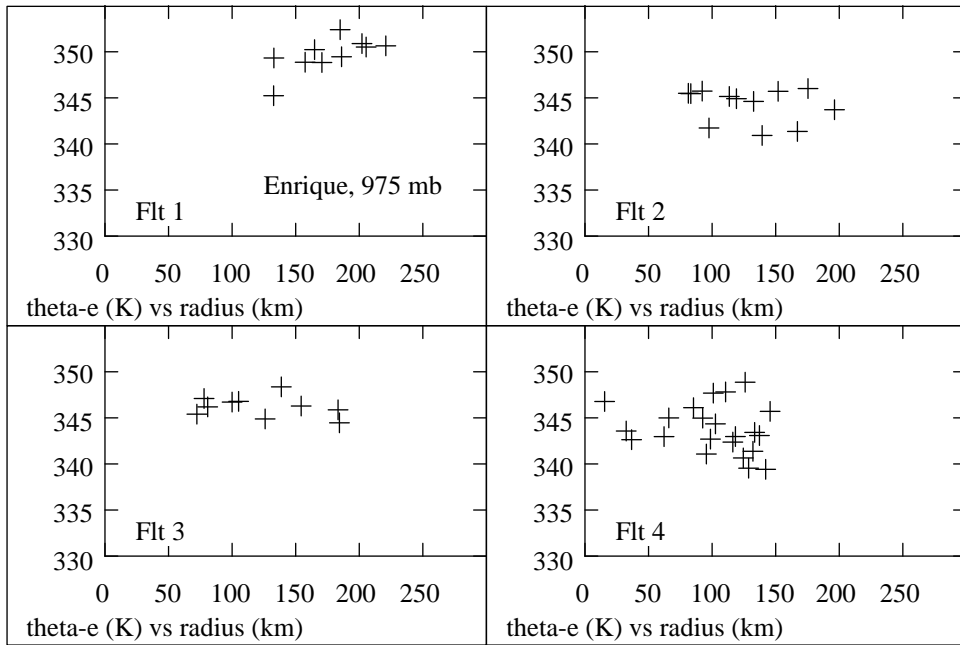


Figure 13: Scatter plot of equivalent potential temperature at 975 mb as a function of distance from the vortex center for flights 1-4 of IOP-2.

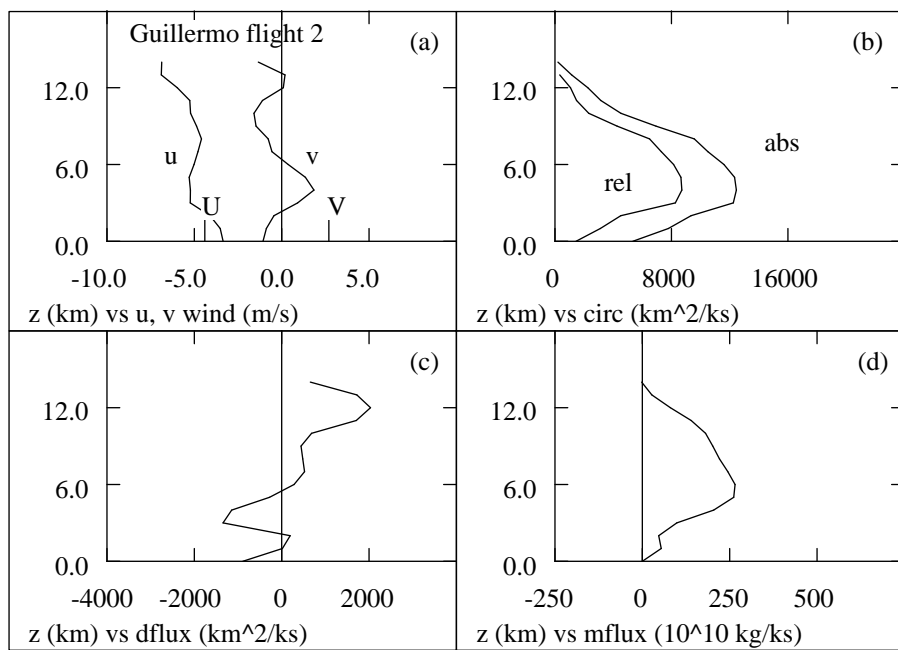


Figure 14: As in figure 10, except flight 2 of IOP-5, near day 215.1.

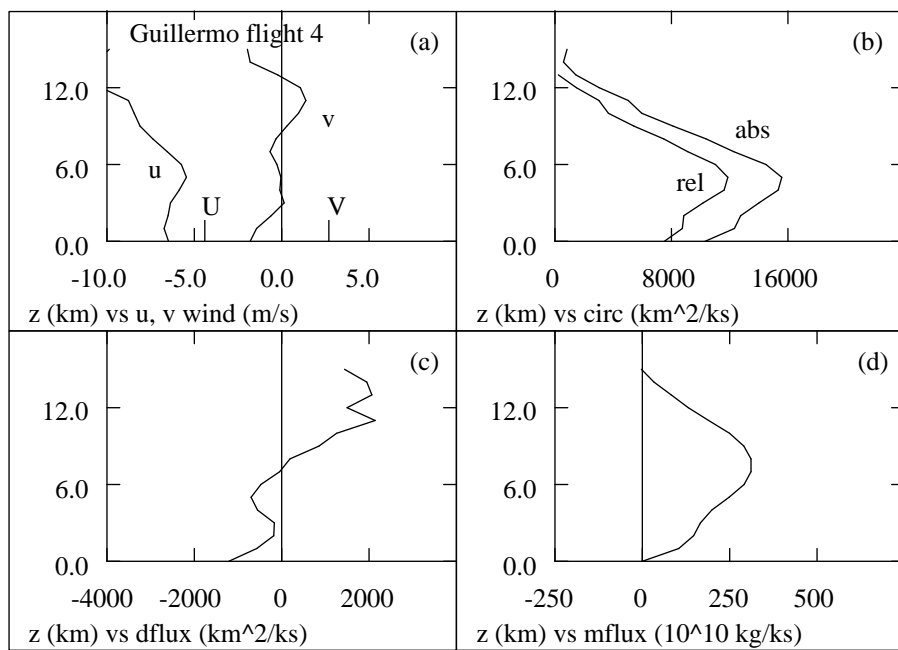


Figure 15: As in figure 10, except flight 4 of IOP-5, near day 216.3.

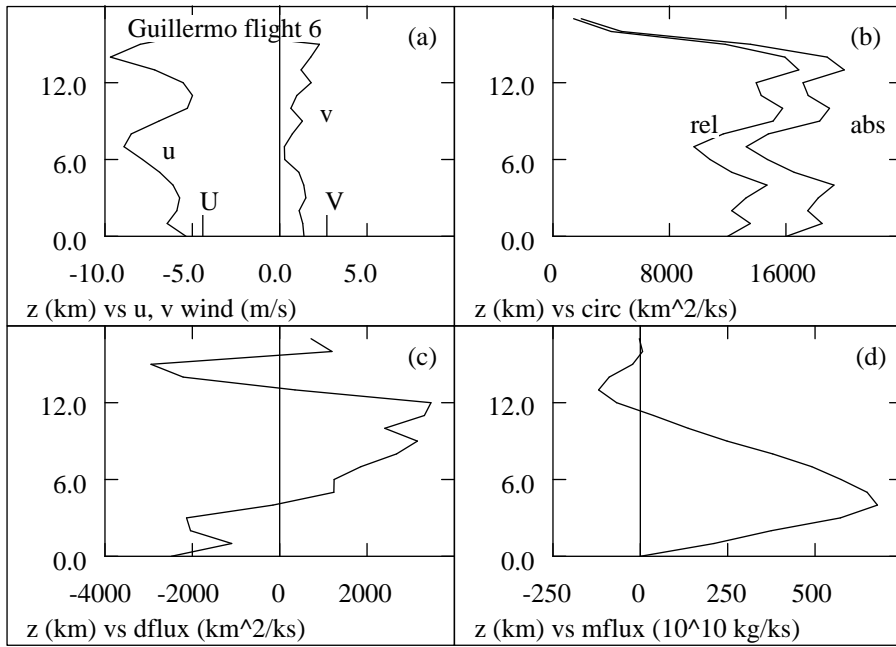


Figure 16: As in figure 10, except flight 6 of IOP-5, near day 217.4.

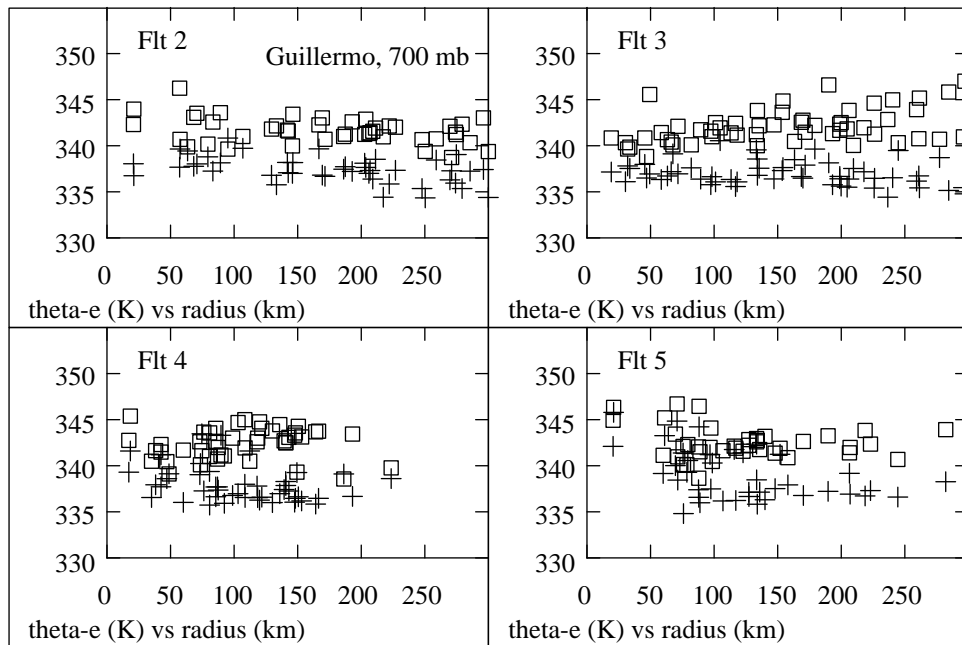


Figure 17: Scatter plot of equivalent potential temperature (crosses) and saturated equivalent potential temperature (squares) at 700 mb as a function of distance from the vortex center for flights 2-5 of IOP-5.

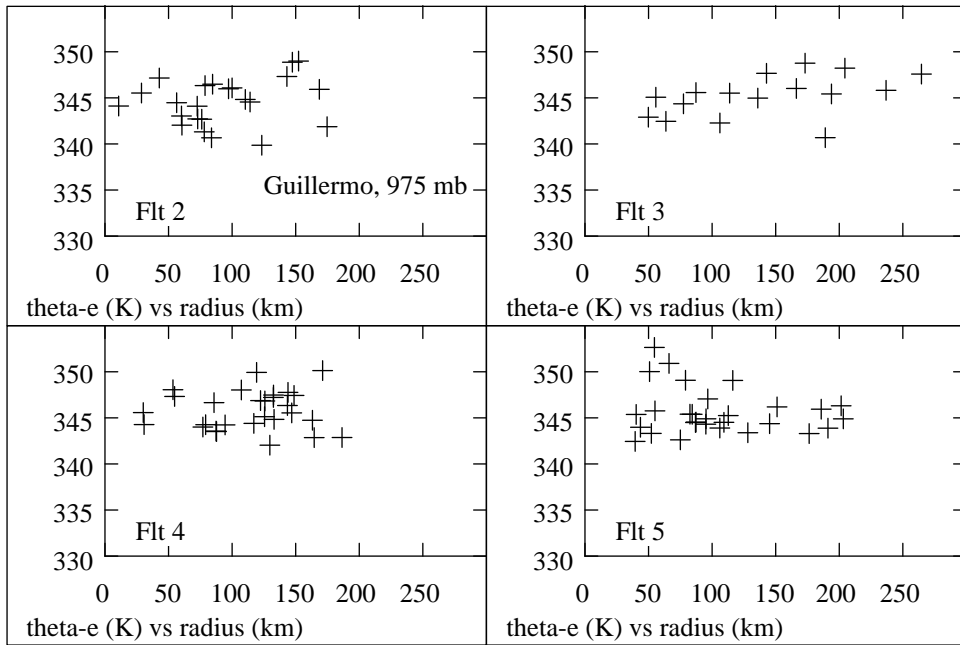


Figure 18: Scatter plot of equivalent potential temperature at 975 mb as a function of distance from the vortex center for flights 2-5 of IOP-5.

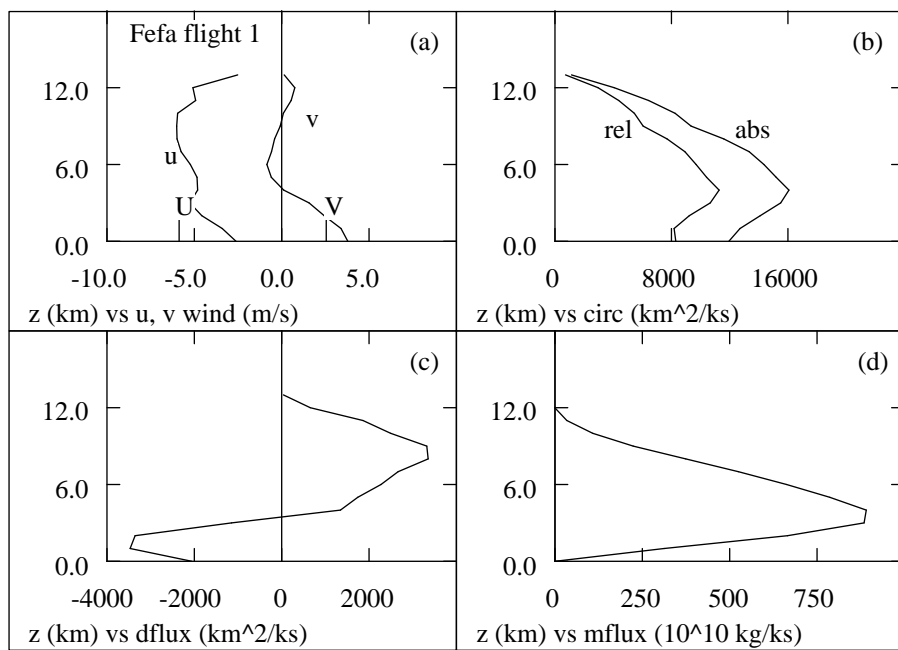


Figure 19: As in figure 10, except flight 1 of IOP-4, near day 210.0.

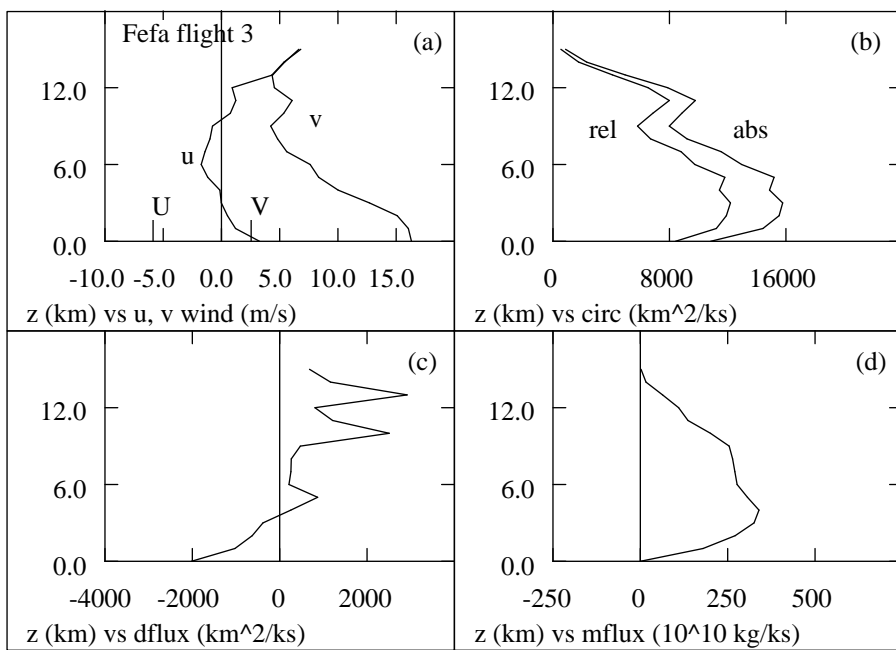


Figure 20: As in figure 19, except flight 3 of IOP-4, near day 211.1.

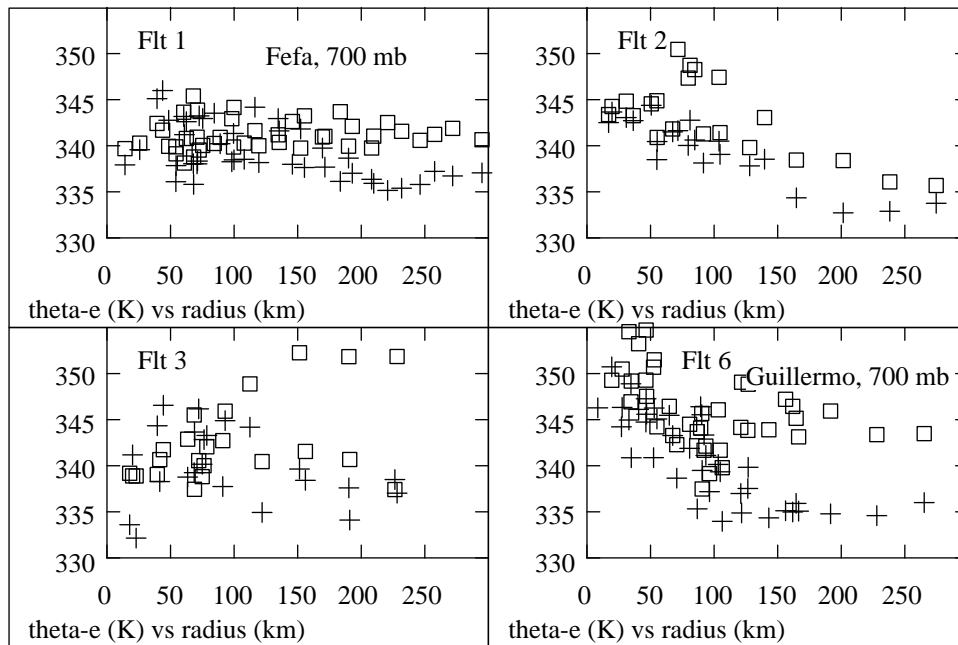


Figure 21: Scatter plot of equivalent potential temperature (crosses) and saturated equivalent potential temperature (squares) at 700 mb as a function of distance from the vortex center for flights 1-3 of IOP-4 and flight 6 of IOP-5.

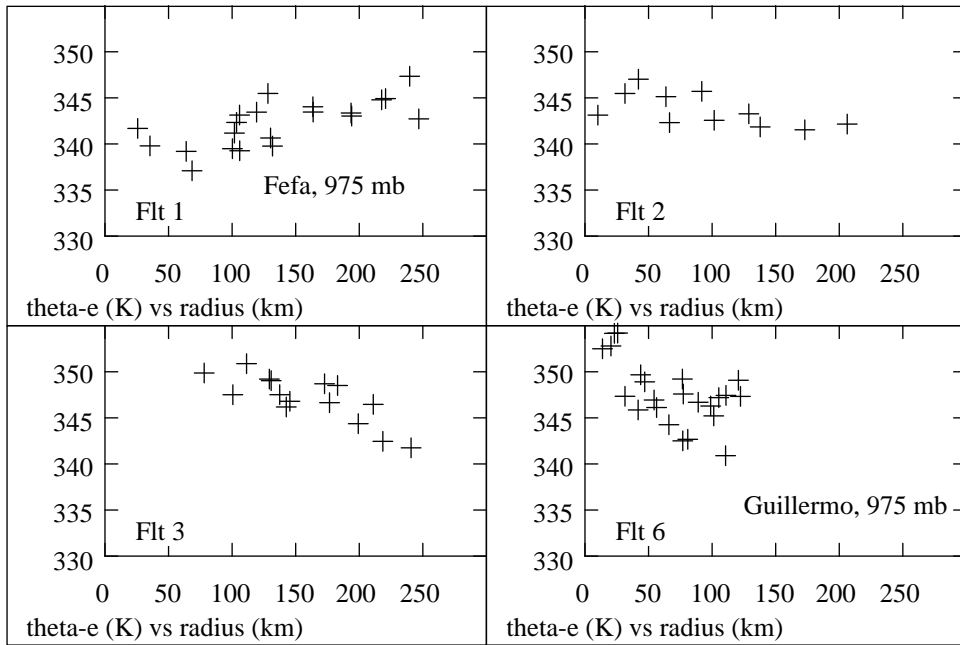


Figure 22: Scatter plot of equivalent potential temperature at 975 mb as a function of distance from the vortex center for flights 1-3 of IOP-4 and flight 6 of IOP-5.

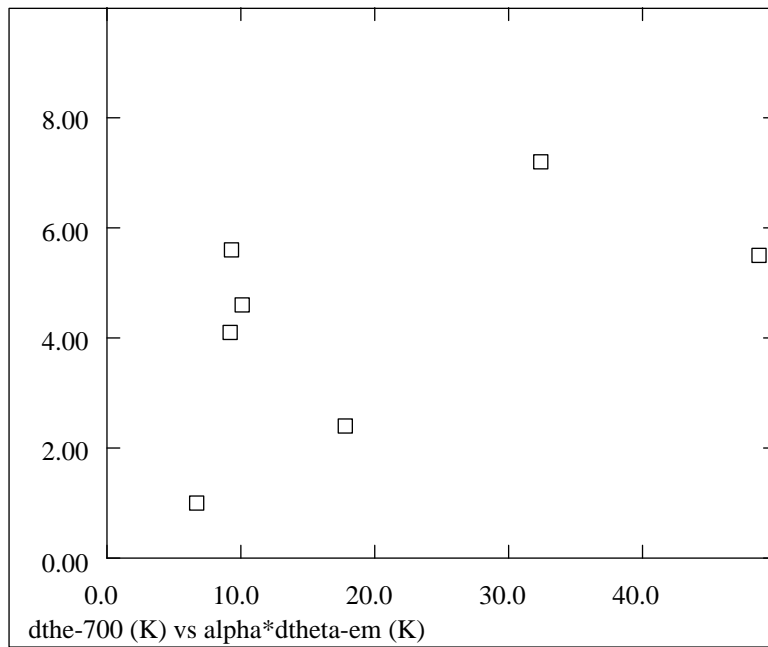


Figure 23: Plot of  $\delta \theta_{e-700}$ , inferred from thermodynamic data, vs  $\alpha \delta \theta_{em}$ , inferred from radar data. See text for further explanation.